Paleoceanography and Paleoclimatology

Supporting Information for

Variable Stoichiometry Effects on Glacial/Interglacial Ocean Model Biogeochemical Cycles and Carbon Storage

Nathaniel J. Fillman[1], Andreas Schmittner[1], and Karin F. Kvale[2]

[1]College of Earth, Ocean, and Atmospheric Sciences, Oregon State University, Corvallis, OR, USA.
[2]Environmental Processes and Modelling, GNS Science, Lower Hutt, New Zealand.

Contents of this file

Introduction

We provide, here, further model validation and performance analysis against observed ocean biogeochemical datasets (Text S1, Figure S1–S7, and Table S1). Text S2 (Figures S8-S13 and Table S2) provides necessary model outputs to support and evidence statements made in the main text. Text S3 presents explicit modeled carbon inventory quantifications and distributions (Figures S14-S18 and Tables S3-S5), while further exploring the diatom model effects on ocean carbon stocks in Text S3.1. Text S4 explores the sensitivity of selected variable stoichiometry models to tertiary simulated biogeochemical processes (Figure S19 and Table S6). Text S5 compares simulated nitrogen isotopes to observed preindustrial and Last Glacial Maxima datasets (Figures S20-S25, Table S7). Lastly, Text S6 describes the relevant biogeochemical equations implemented or altered in the model (University of Victoria, Earth System Climate Model – Model of Ocean Biogeochemistry and Isotopes) for the variable stoichiometry configuration (Table S8).

Text S1. Variable Stoichiometry and Nutrient Simulations

S1.1: Statistical Performance of Simulated Surface Nutrients

Table S1 summarizes statistical metrics of the simulated nutrient distributions relative to observed data from the World Ocean Atlas, 2013 (Garcia et al., 2013; Letscher et al., 2013; Mather et al., 2008). R is the correlation coefficient; the *Tuned* experiment, here, generally outperforms all other simulations except forNO_3 where it is slightly less accurate than the *Control*. STDR expresses the ratio of standard deviations of the model data to observations measuring how well the model captures the natural variability. The *Tuned* model again performs the best comprehensively, except with the PO_4 simulations. Here, all model configurations struggle with the *Control* simulation capturing the variance best. However, out of the three variable stoichiometry model (VSM) configurations, the *Tuned* model is the most accurate. RMSE is the uncertainty-corrected root mean square error where the *Tuned* model configuration has the smallest error, but it is approximately matched by the *Control* experiment in the NO_3 simulations. Lastly, the RMS Prime is essentially the same as the RMSE but the bias of the global means of the observations and the models have been removed. The RMS Prime values are all exceedingly similar to the RMSE indicating the model global averages are all similar to the observed global mean. These statistical calculation methods were developed and described in Muglia et al. (2018).

Table S1. PI Surface (0-120 m) Nutrient Statistical Assessment.

NO_3	**R**	**STDR**	**RMS prime**	**RMSE**
Control	0.89	0.96	0.46	0.49
VarP:N	0.86	1.12	0.58	0.58
VarSi:N	0.86	1.17	0.60	0.60
Tuned	0.89	1.02	0.48	0.49
PO_4	**R**	**STDR**	**RMS prime**	**RMSE**
Control	0.89	0.92	0.45	0.48
VarP:N	0.89	0.86	0.46	0.55
VarSi:N	0.89	0.85	0.46	0.54
Tuned	0.90	0.89	0.44	0.48
Si	**R**	**STDR**	**RMS prime**	**RMSE**
Control	0.86	1.27	0.64	0.66
VarP:N	0.87	1.25	0.63	0.64
VarSi:N	0.90	1.00	0.44	0.47
Tuned	0.91	0.99	0.43	0.47

S1.2: Global Maps of Surface Nutrients

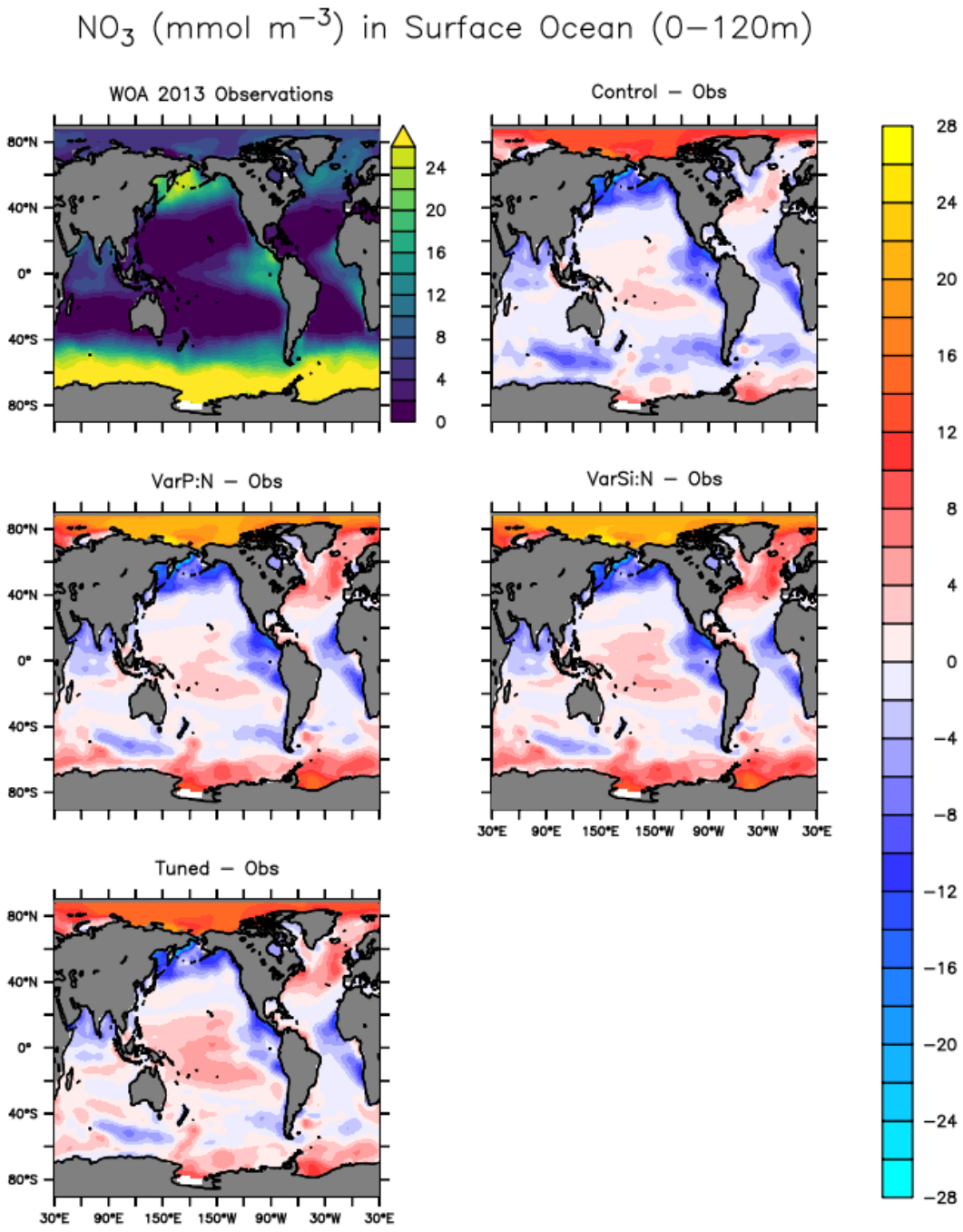

Figure S1. Surface Nitrate comparison.

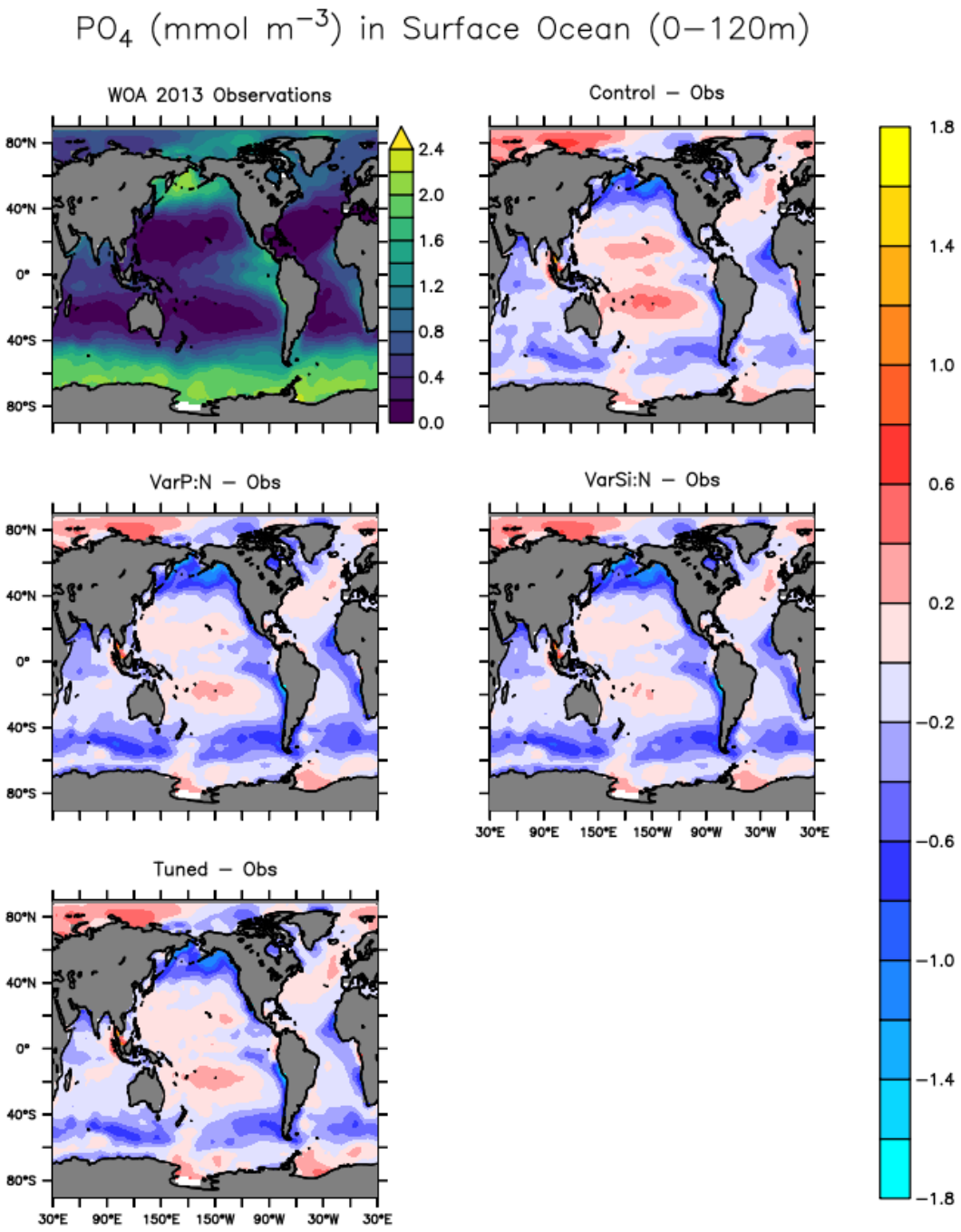

Figure S2. Surface Phosphate comparison.

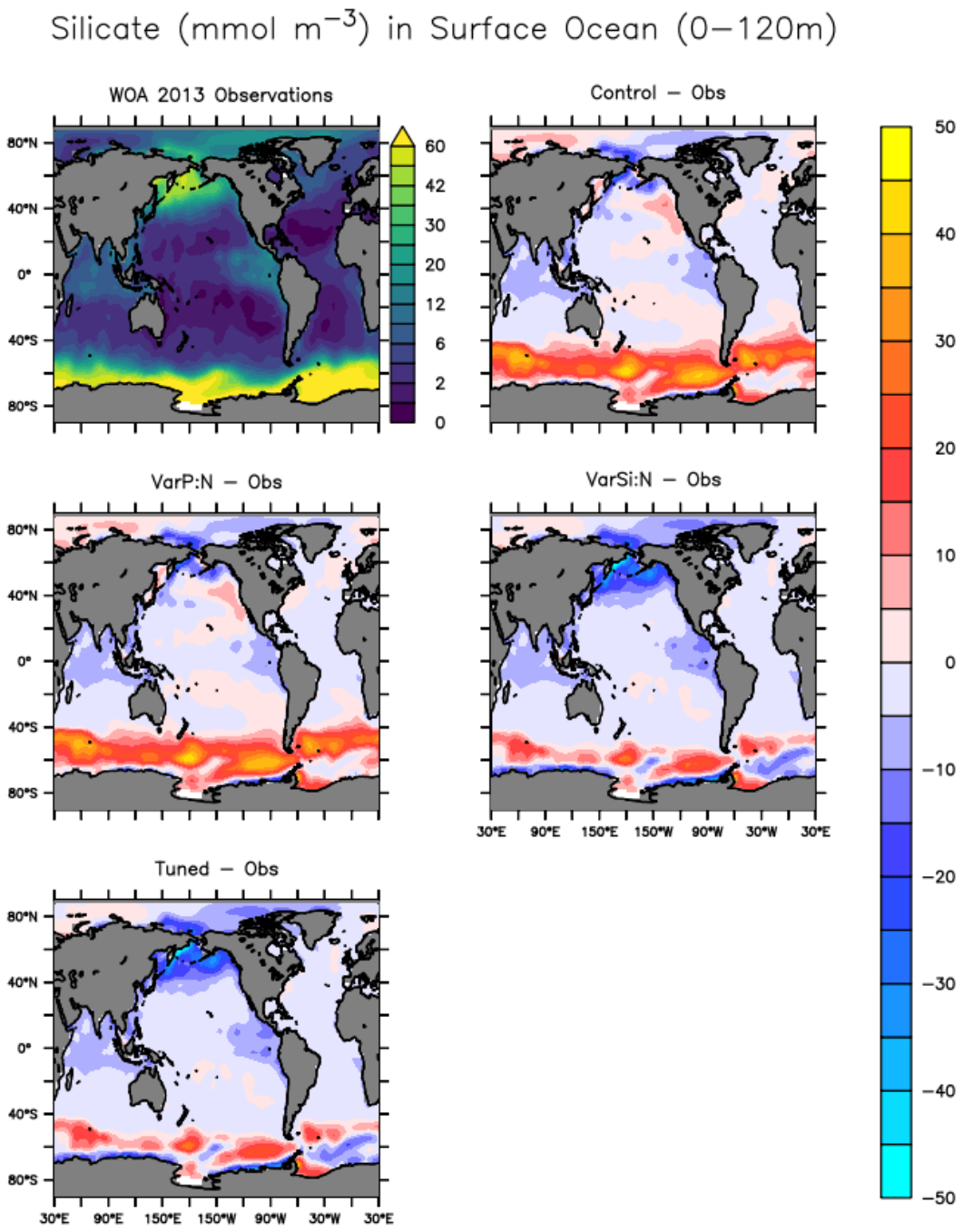

Figure S3. Surface Silicate comparison.

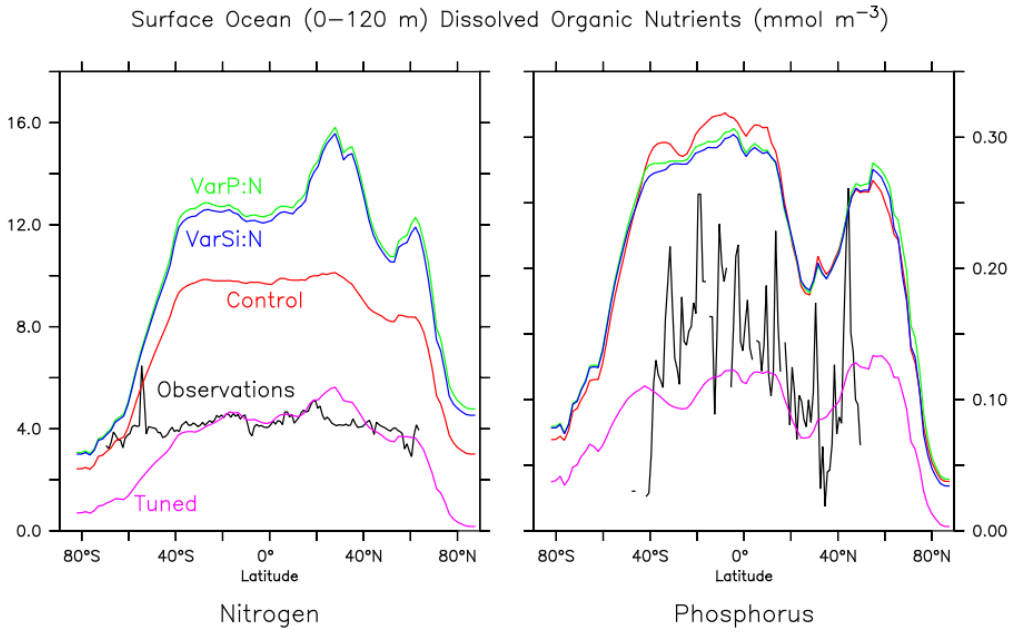

Figure S4. Dissolved organic nutrients, zonally averaged, with nitrogen (left) and phosphorus (right) in the surface ocean (0 – 120 m). Remineralization rates were increased 5-fold, resulting in the Tuned simulation better approximating the observations.

S1.3: N* Comparison and Analysis

N* is defined as (Gruber & Sarmiento, 1997; Sarmiento & Gruber, 2006):

$$N^* = NO_3 - 16 \times PO_4 + 2.9\ (mmol\ m^{-3}) \tag{S1}$$

Calculating the absolute value of differences for N* comparisons:

$$|\Delta N^*| = |N^*_{model} - N^*_{obs}| = |(NO_3^{model} - 16 \times PO_4^{model}) - (NO_3^{obs} - 16 \times PO_4^{obs})| \tag{S2}$$

$$= |NO_3^{model} - NO_3^{obs} - 16 \times PO_4^{model} + 16 \times PO_4^{obs}|$$

$$= |(NO_3^{model} - NO_3^{obs}) - (16 \times PO_4^{model} - 16 \times PO_4^{obs})|$$

$$= |\Delta NO_3 - 16 \times \Delta PO_4|$$

Therefore, in the case that $\Delta NO_3 = 0$, ΔPO_4 exclusively causes ΔN^*:

$$|\Delta N^*| - |16 \times \Delta PO_4| = 0$$

Conversely, if $\Delta PO_4 = 0$, ΔNO_3 exclusively causes ΔN^*:

$$|\Delta NO_3| - |\Delta N^*| = 0$$

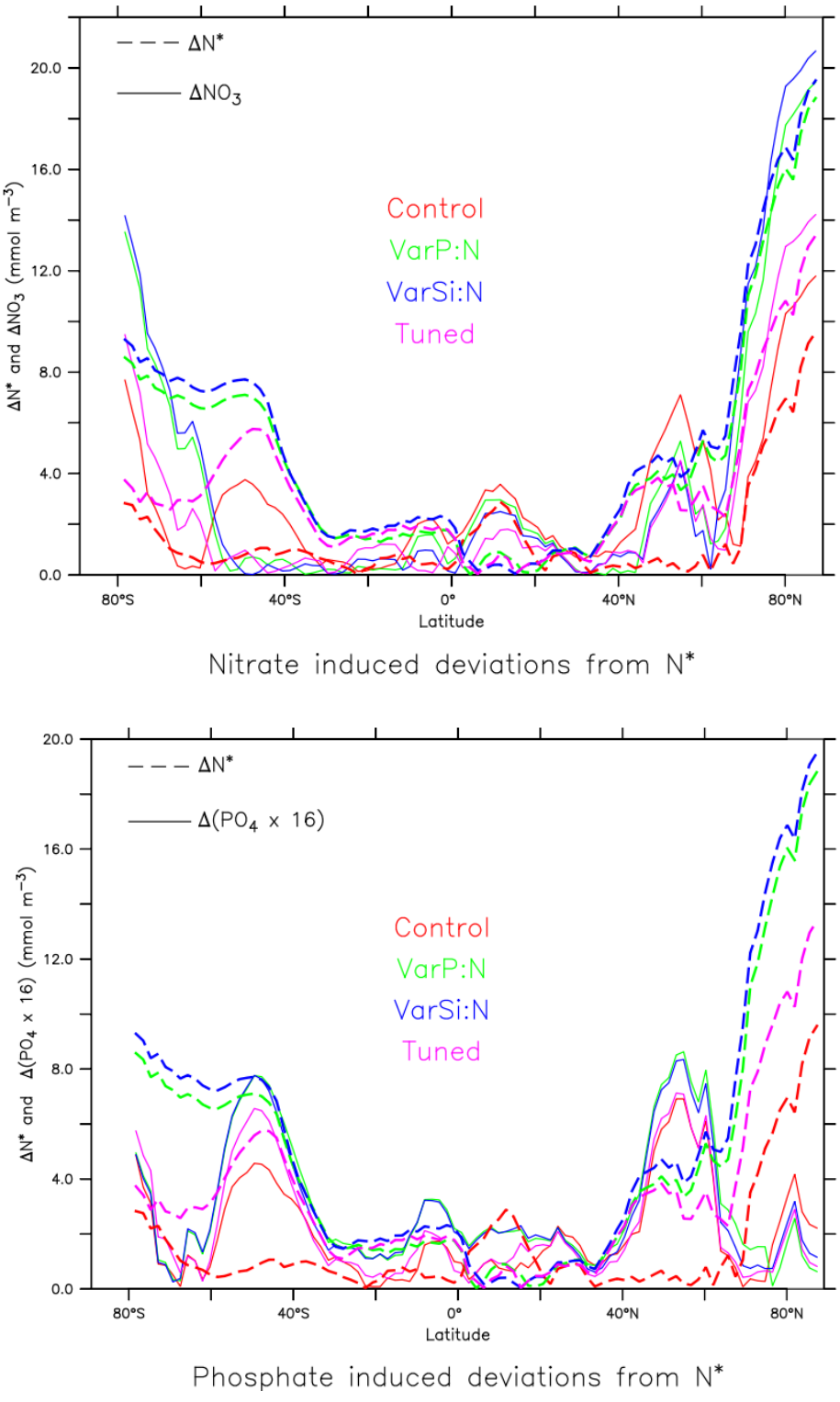

Figure S5. Deviations from observed zonally averaged N* values in each experiment caused by NO_3 (top) or PO_4 (bottom) simulation inaccuracies. The dashed lines show the absolute magnitude of the difference in N* between the observations and a given

experiment, whereas the solid lines show the NO_3 or PO_4 contribution to that difference. Thus, when two lines of a given color overlap, the corresponding nutrient is fully responsible for the N* deviation. See Equation S1 and S2, for calculation of N* differences.

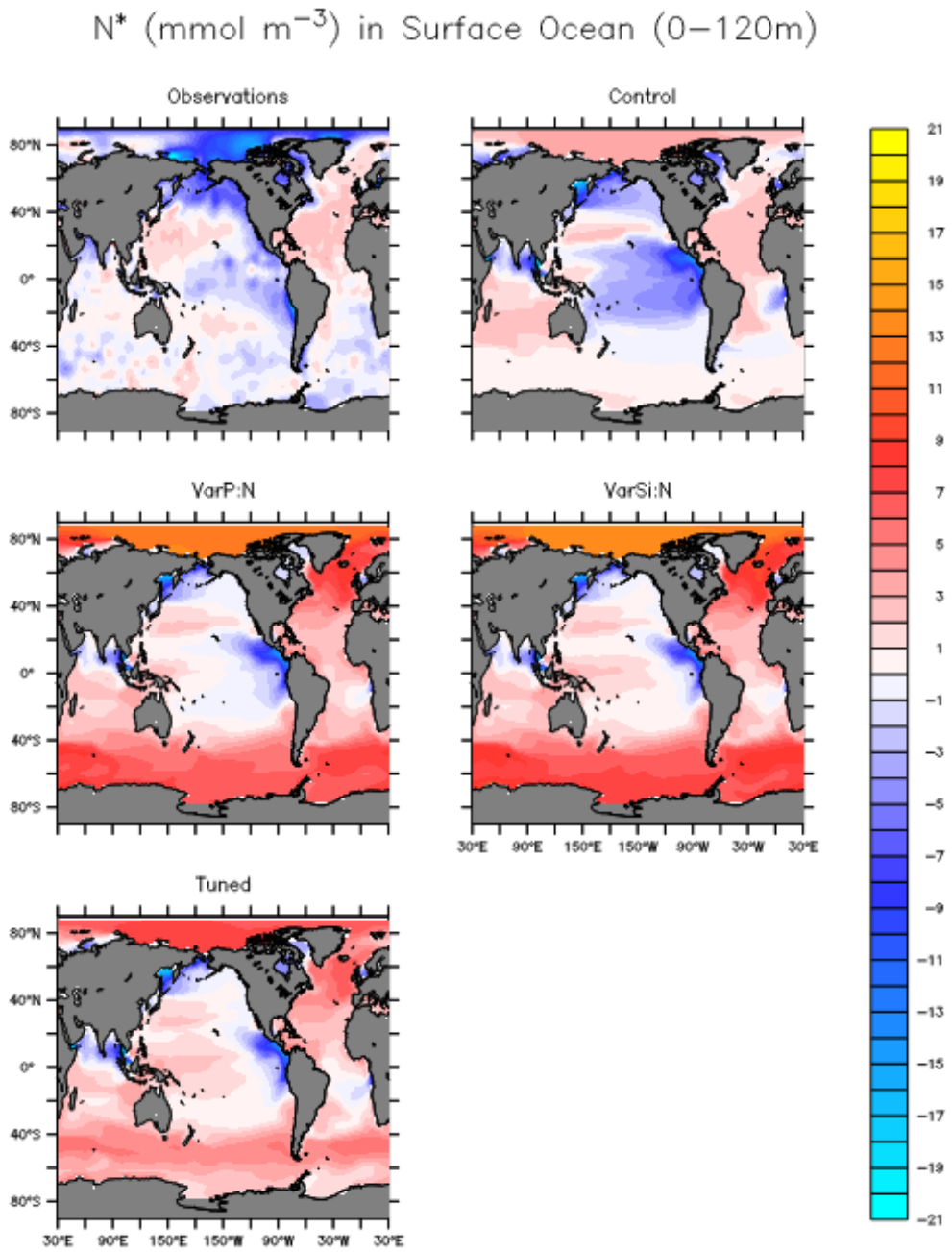

Figure S6. N* calculated from observation and simulations in the surface ocean (0 – 120 m). See Equation S1.

S1.4: Vertical Profiles of O_2 and NO_3

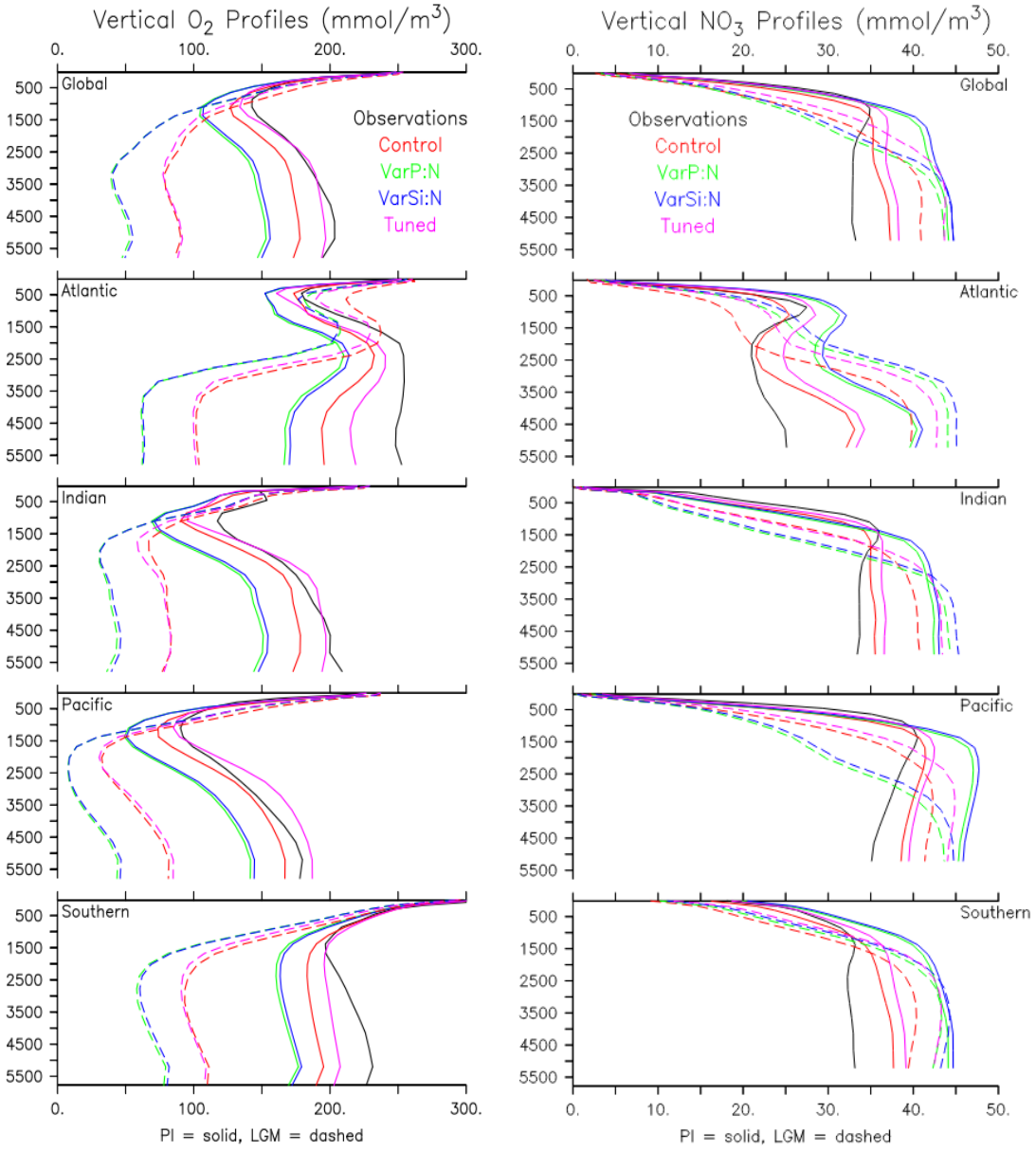

Figure S7. Vertical profiles of horizontally averaged O_2 and NO_3 in each ocean basin.

Text S2. Primary Producer Responses

S2.1: Global Limiting Nutrient Maps

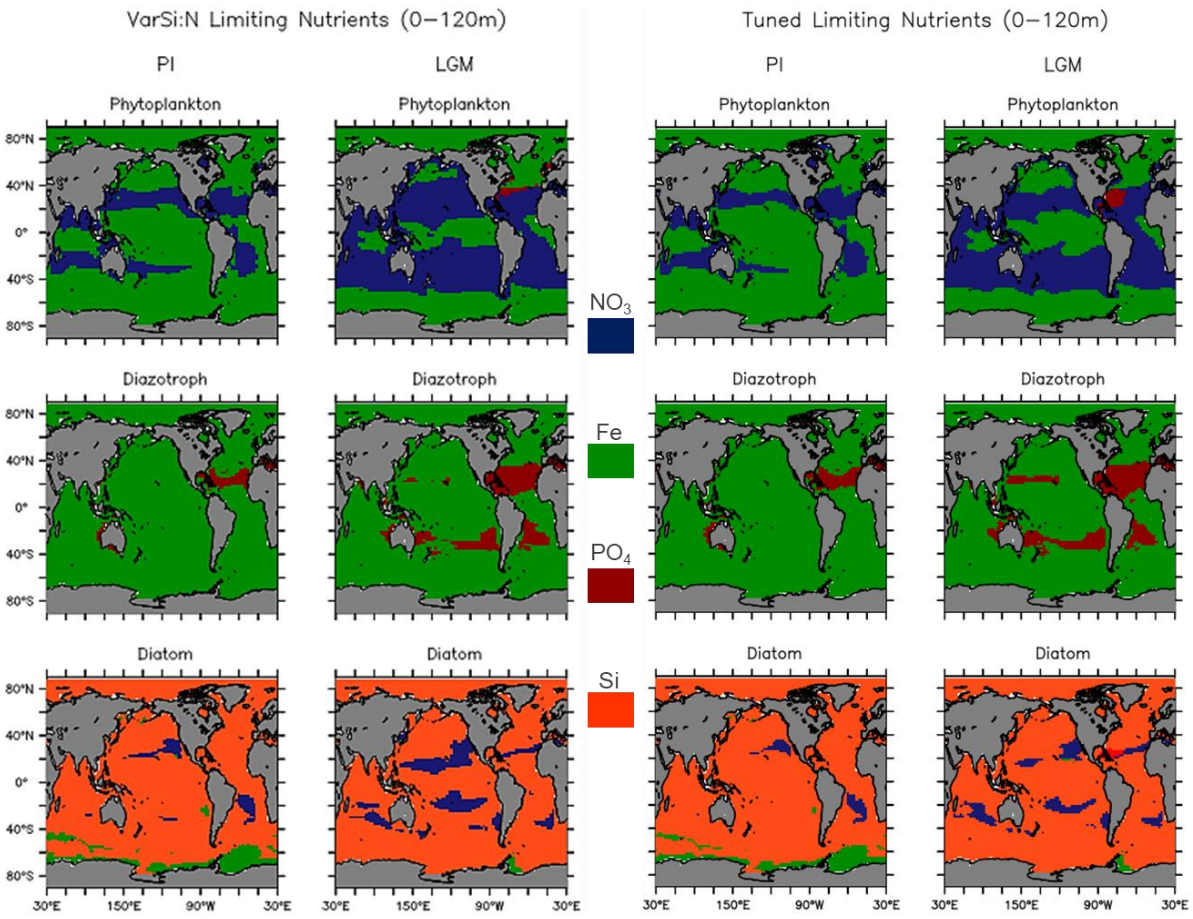

Figure S8. Primary limiting nutrients for each PFT in the surface ocean (0 – 120m). The accelerated DOM remineralization in Tuned decreases the P_O and P_{Diat} N limitation. Comparing VarSi:N to VarP:N (Figure 11), the P_{Diat} Si limitation is increased. The dustier LGM tends to decrease the Fe limitation for all between the PI and LGM simulations.

S2.2: NPP

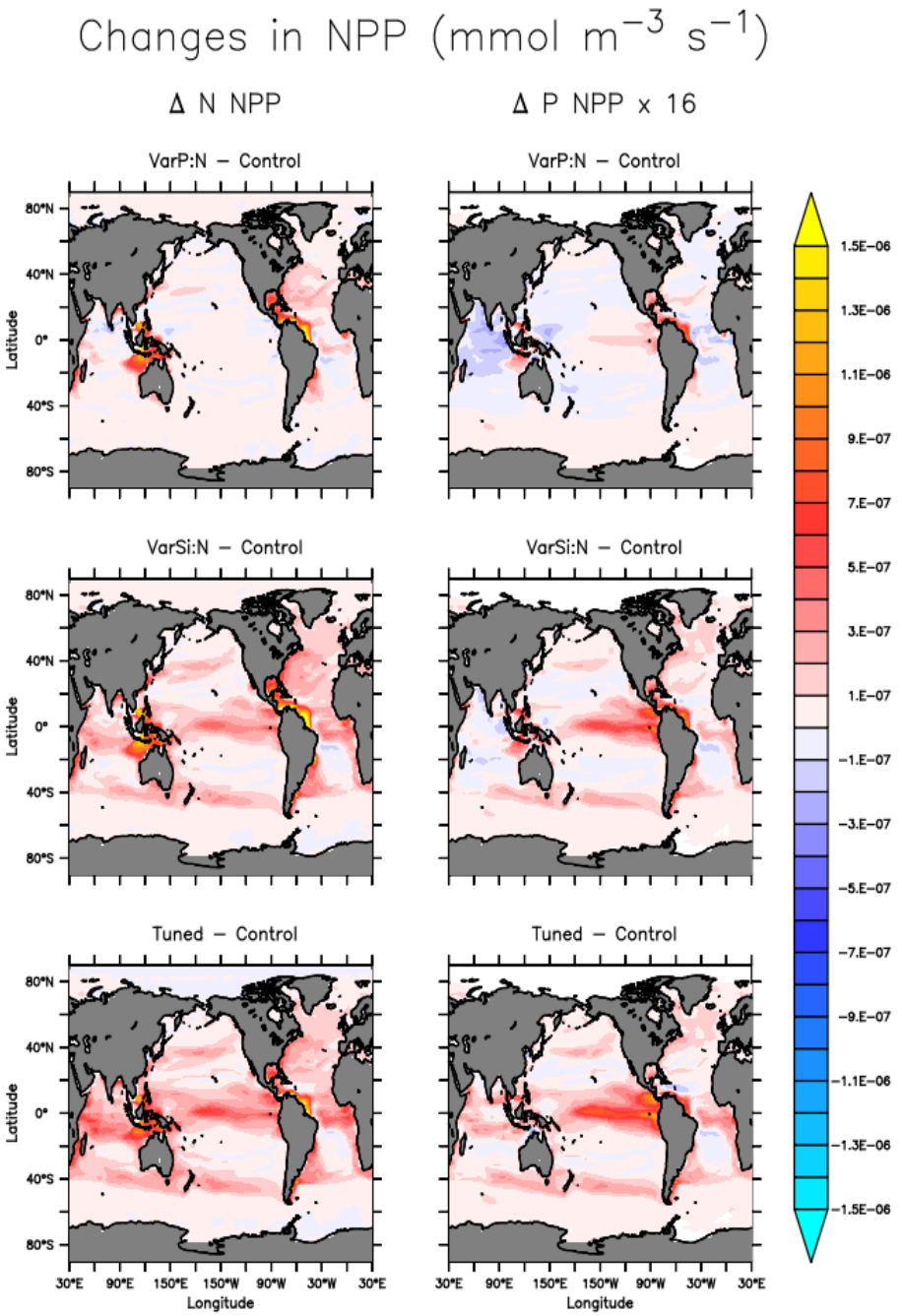

Figure S9. Changes in PI P_O NPP between a given experiment and the Control. The left column of plots are the changes of NPP in N units, while the right are plots for P units recast (by a factor of 16) into pseudo-N units for easier comparison.

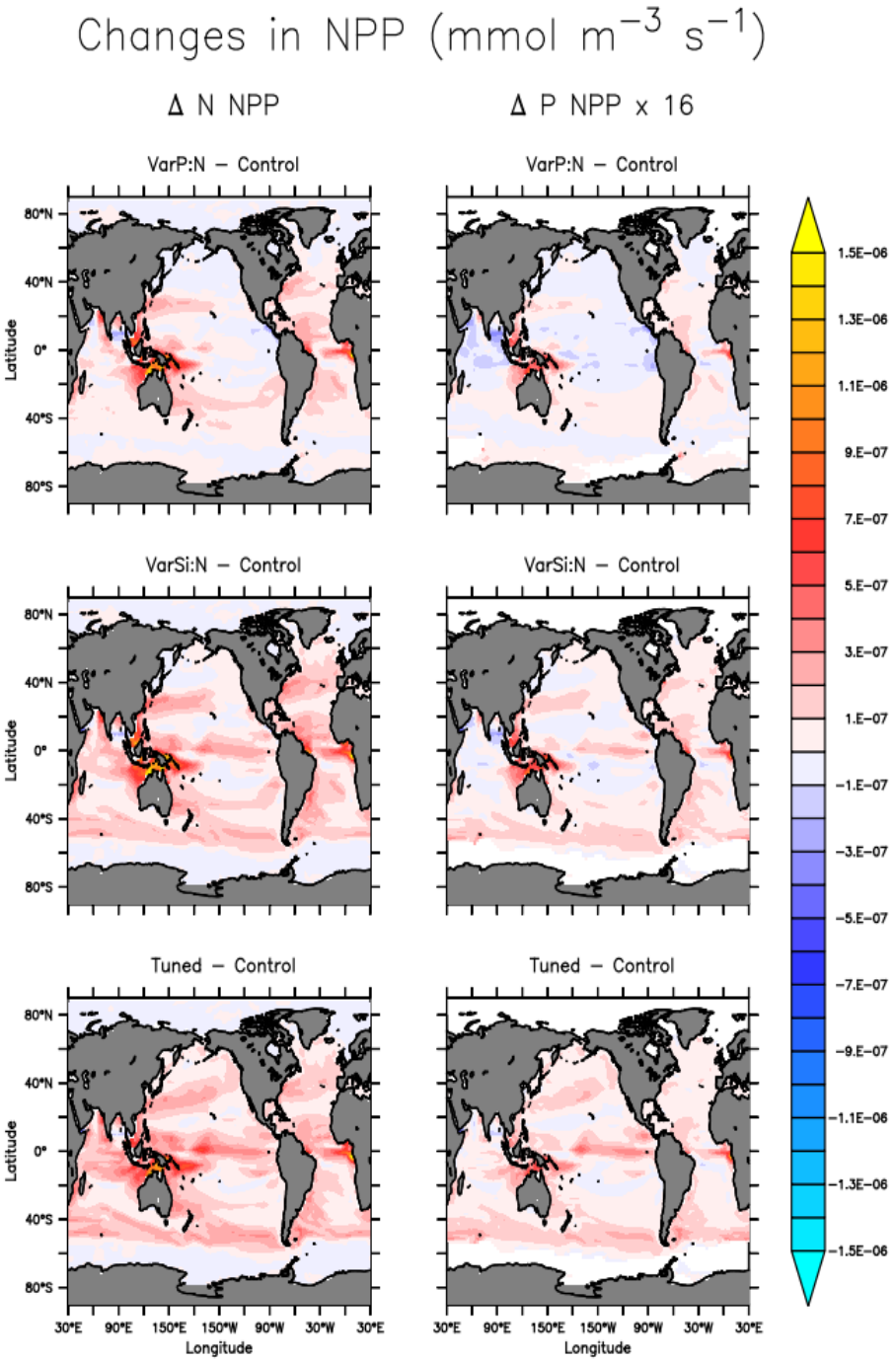

Figure S10. Changes in LGM P_O NPP between a given experiment and the Control. The left column of plots are the changes of NPP in N units, while the right are plots for P units recast (by a factor of 16) into pseudo-N units for easier comparison.

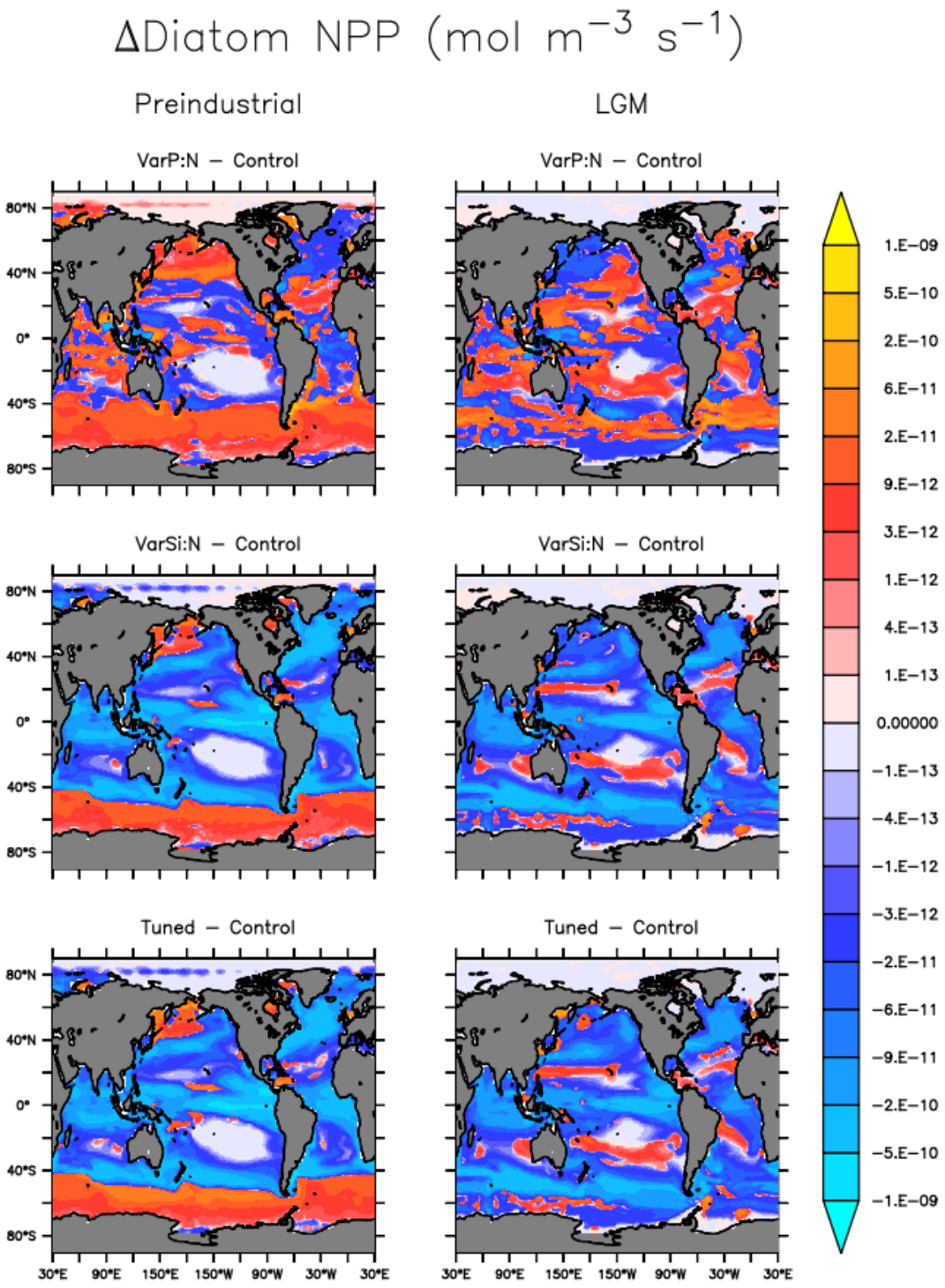

Figure S11. Changes in Diatom NPP in response to VarP:N (top row), VarSi:N (middle Row), and Tuned (bottom row) in the surface ocean (0-120 m) during the PI (left column) and LGM (right column). Note the logarithmic color scale.

S2.3: Relative Abundances

Table S2. Globally integrated plankton biomasses and relative abundances.

	Relative abundance (%)			Biomass (N Tmol)			
PI	**P_O**	**P_{Diaz}**	**P_{Diat}**	**P_O**	**P_{Diaz}**	**P_{Diat}**	**P_Z**
Control	44.1	1.9	54.0	4.0	0.2	4.9	5.7
VarP:N	54.8	3.7	41.5	6.4	0.4	4.9	5.5
VarSi:N	66.4	3.8	29.7	7.6	0.4	3.4	5.5
Tuned	66.9	2.9	30.2	7.6	0.3	3.4	5.7
LGM							
Control	41.5	2.0	56.6	3.1	0.2	4.2	4.7
VarP:N	58.6	4.5	36.9	6.7	0.5	4.2	4.4
VarSi:N	68.7	4.7	26.7	7.6	0.5	2.9	4.5
Tuned	69.5	3.3	27.2	7.5	0.4	2.9	4.6

Note. Relative abundances were calculated as the ratio of one PFT's biomass to the total biomass of all primary producers, excluding all zooplankton and detritus.

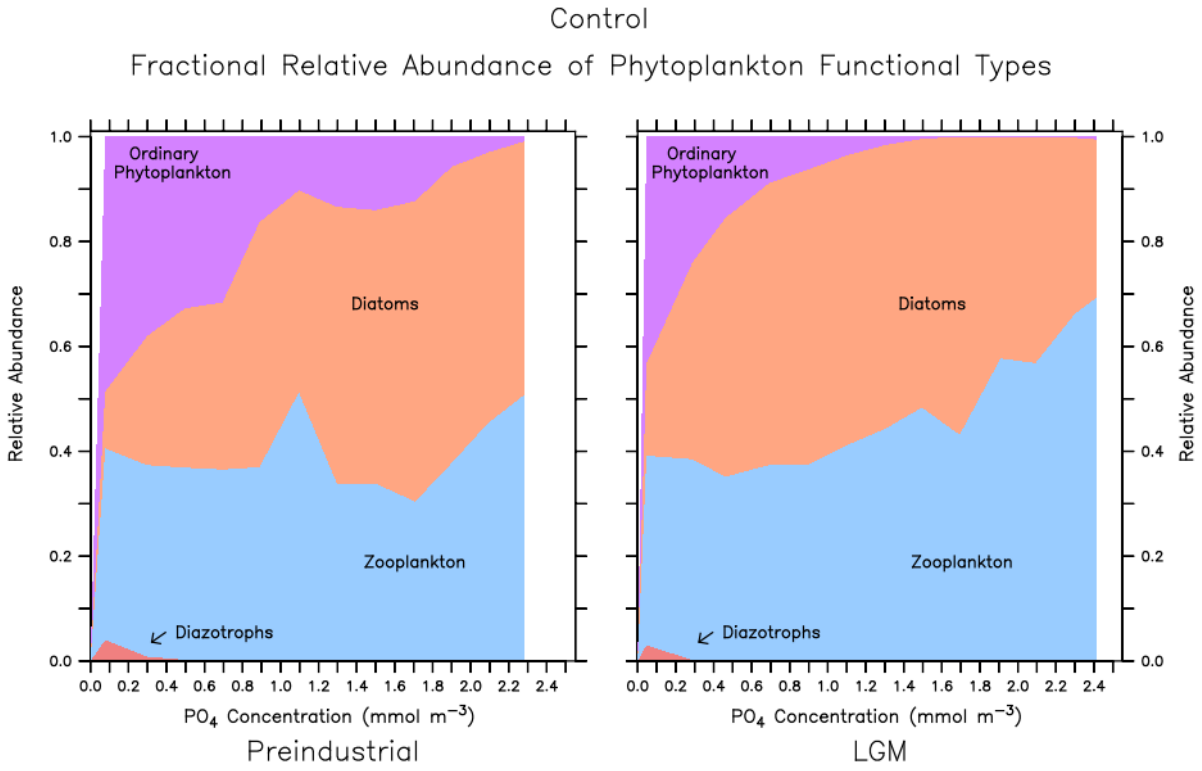

Figure S12. The relative abundance of each PFT against surface ocean (0-120 m) PO_4 concentrations in the Control.

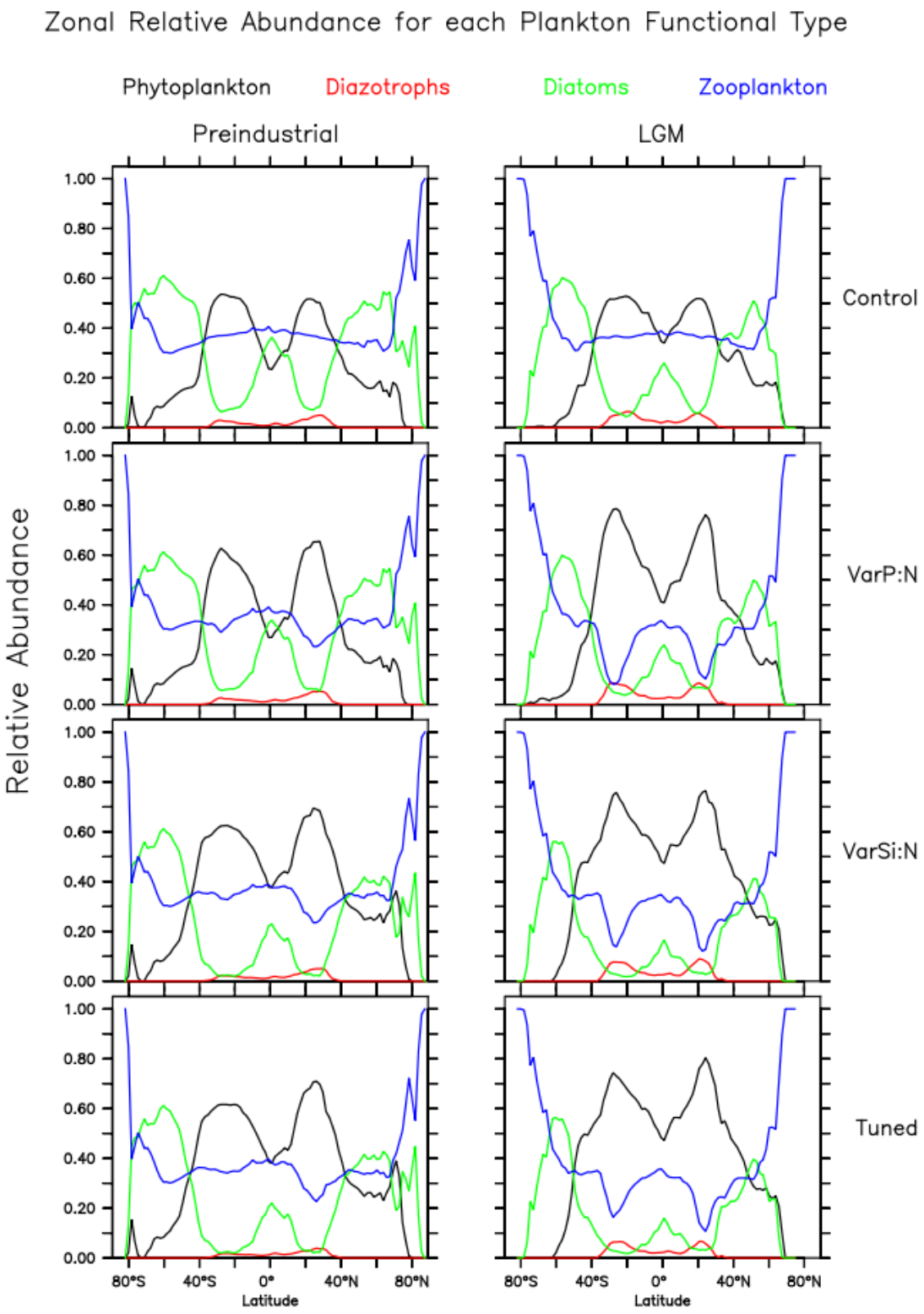

Figure S13. Zonally averaged relative abundance of each PFT in the surface ocean (0-120 m) in the PI (left column) and LGM (right column) oceans.

Text S3. Carbon Export Production and Associated Variables

Table S3. Global Carbon quantifications.

PI	pCO_2 (ppm)	pCO_2 (Pg)	Ocean total carbon (Pg)	Ocean DIC (Pg)	Ocean DOC (Pg)	Ocean POC (Pg)	DIC:Alkalinity (surface average)	Land carbon (Pg)
Control	273.3	573.9	37956	37674	280.1	1.5	0.8623	1808
VarP:N	274.9	577.3	38366	37978	385.6	1.7	0.8621	1812
VarSi:N	274.7	576.9	38255	37877	376.1	1.7	0.8623	1811
Tuned	273.3	573.9	37505	37447	56.9	1.7	0.8623	1808
LGM								
Control	204.7	429.9	38174	37931	242.0	1.3	0.8464	1334
VarP:N	193.3	405.9	38662	38273	387.5	1.6	0.8427	1287
VarSi:N	192.1	403.4	38558	38184	372.4	1.6	0.8426	1282
Tuned	190.5	400.1	37813	37754	57.4	1.6	0.8418	1276

Note. Land C does not include the 402 Pg of C buried under the ice in the LGM.

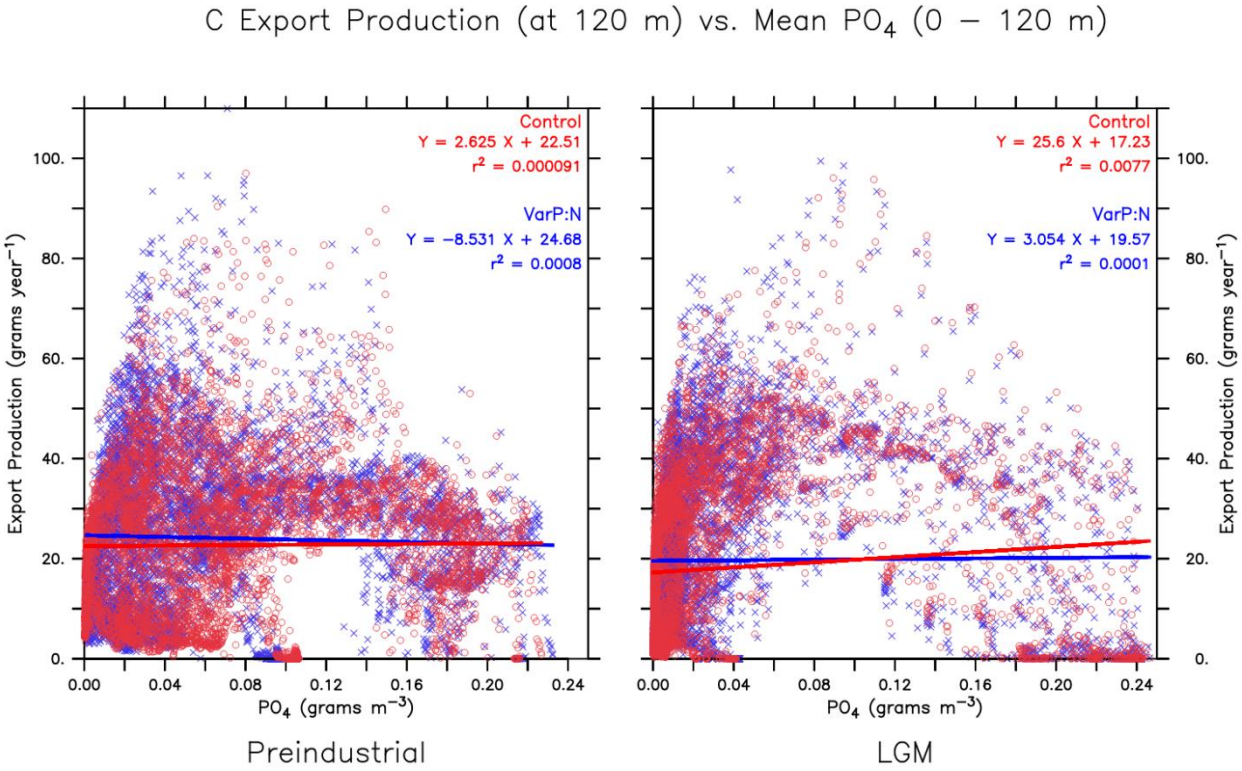

Figure S14. The relationship between C export and PO_4, which is used as a metric for oligotrophy. The PI is on the left with the Control in red and VarP:N in blue. The right is the same for the LGM. Based on the trendlines, VarP:N exports more C than the Control at low PO_4. This holds for most of the PI ocean but is only valid up to 1.0 g PO_4 m^{-3} in the LGM. However, more LGM grid points have low PO_4 than high. Thus, VarP:N

exports more C than the Control. Many other nutrient (NO_3, Fe, etc.) and environmental (light, temperature, etc.) variables regulate C export, hence the low r^2 values.

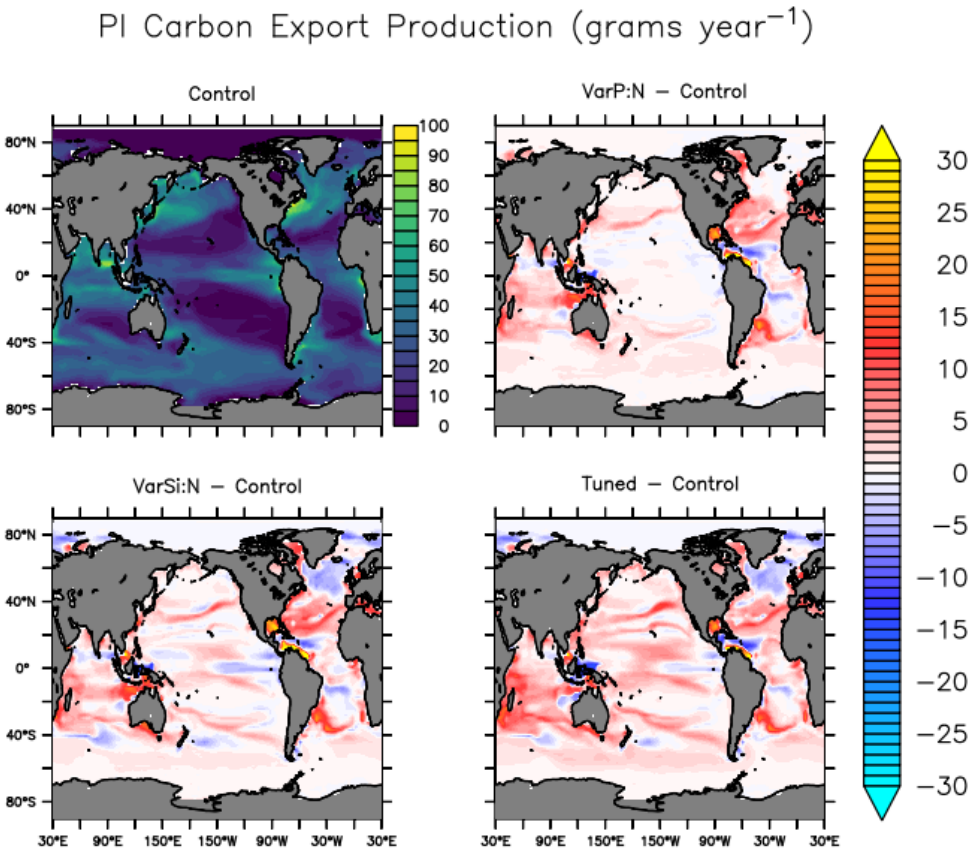

Figure S15. Carbon Export Production in the PI Control simulation with changes induced by the VSMs.

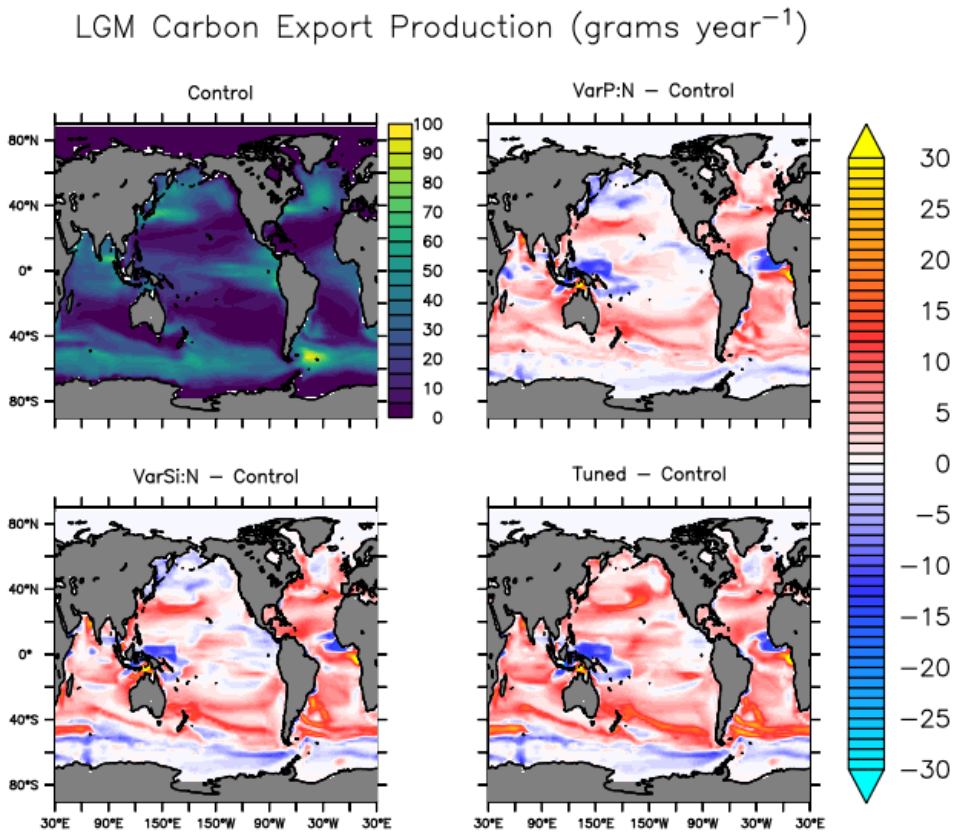

Figure S16. Carbon Export Production in the LGM Control simulation with changes induced by the VSMs.

Table S4. Linearized approximations of changes in DOC fluxes.

LGM – PI (Pg C year^{-1})	**Control**	**VarP:N**	**VarSi:N**	**Tuned**	**VarP:N - Control**	**VarSi:N - Control**	**Tuned - Control**
$\mu^*_{P_O}(\Delta P_O)$	-0.07	0.04	0.01	0.01	0.11	0.08	0.08
$\Delta(\upsilon_{P_O} P_O T_S)$	-0.18	-0.09	-0.18	-0.19	0.08	0.00	-0.02
$\upsilon_{P_O}(\Delta P_O) T_S$	-0.11	0.08	0.01	-0.01	0.19	0.12	0.10
$\upsilon_{P_O} P_O(\Delta T_S)$	-0.08	-0.15	-0.18	-0.18	-0.08	-0.10	-0.10
$\Delta(\lambda_{DOC}[DOC]T_S)$	-0.46	-0.27	-0.31	-0.33	0.19	0.15	0.13
$\lambda_{DOC}[DOC](\Delta T_S)$	-0.26	-0.39	-0.38	-0.38	-0.13	-0.13	-0.13
$\lambda_{DOC}(\Delta[DOC])T_S$	-0.25	0.11	0.06	0.04	0.37	0.32	0.29
Average Temperature (°C)	-2.16	-2.27	-2.28	-2.28	-0.12	-0.13	-0.12

Note. Selected variables are the P_O specific (μ^*) and quadratic (υ) mortalities (Table S8), the temperature scaling function $T_S=1.066^T$, DOC remineralization (λ_{DOC}), and the average temperature changes. The three right-most columns are the LGM to PI difference of a VSM compared to the same difference in the Control. Both decomposed terms that isolate changes in P_O can be summed for the total P_O effect on DOC and be compared to the corresponding temperature effect.

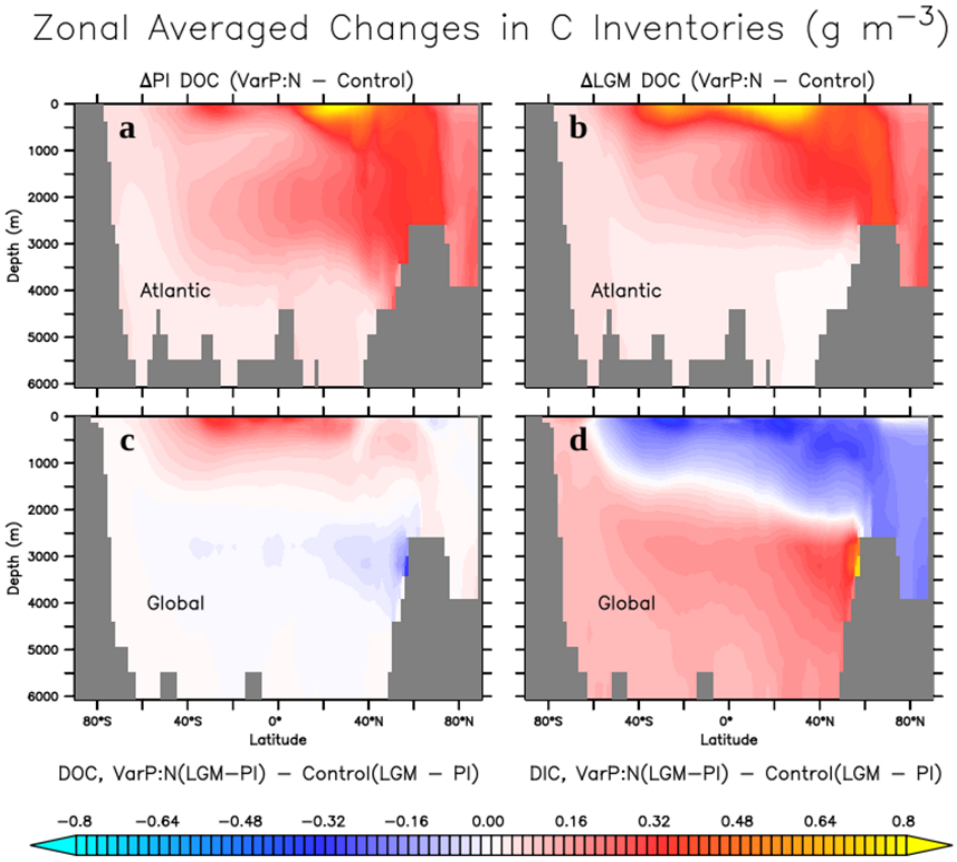

Figure S17. Cross-sections of changes in DIC and DOC. Panels A and B show the VarP:N change in DOC in the PI and LGM Atlantic. The North Atlantic Deep Water (NADW) is visible in DOC's trajectories. Notably, the shoaling of the NADW between the PI and LGM, moves upward the midlatitude deep Atlantic DOC maxima, inducing a negative signature there when comparing the relative LGM-PI DOC changes between VarP:N and Control in Panel C. Panel D the same relative changes but for DIC.

S3.1: Diatom Carbon Export Production.

The amount of P_{Diat}-sourced C that is exported while adhered to the siliceous frustules can be approximated in the following manner. The surface ocean average Fe is weighted by the P_{Diat} biomass and submitted as an argument to the *VarSi:N* model (Equation S4) to calculate the Si:N of P_{Diat}. Once this ratio is divided into the Si export (Si_{EP}), the result describes the ballasted N EP of P_{Diat} as if there were no degradation of soft tissue. Therefore, we subtract off the remineralization and grazing terms from this value (Table S8). It can then be easily converted to C EP using the fixed C:N (Equation S5). The biogenic Si sinking velocity is captured in the Si_{EP} variable.

$$\overline{[Fe]} = \frac{1}{\int_{-120m}^{0} P_{DT}\, dz} \times \int_{-120m}^{0} Fe \times P_{DT}\, dz \quad \text{(S3)}$$

$$Si{:}N\ \left(\frac{mol}{mol}\right) = -\alpha * \tanh\left(\beta * \overline{[Fe]} - \gamma\right) + \varepsilon \quad \text{(S4)}$$

$$P_{DT_{EP}} = \left[\frac{Si_{EP}}{Si{:}N} - (1-\gamma)P_z G^*_{P_{DT}} - (1-\sigma 1_{DOM})\upsilon_{P_{DT}} P_{DT}\right] \times C{:}N \quad \text{(S5)}$$

Otherwise, if all the P_{Diat} soft tissue is disassociated from the faster sinking biomineral, then the P_{Diat}-only portion of the simulated detritus is given as

$$P_{DT_{EP\_soft}} = w_D \acute{\alpha}\left[(1-\gamma)P_z G^*_{P_{DT}} - (1-\sigma 1_{DOM})\upsilon_{P_{DT}} P_{DT}\right] \times C{:}N \quad \text{(S6)}$$

Where $\acute{\alpha}$ is the timestep of biology used in the model and w_D is the sinking velocity of the detritus. The remaining variables are described in Table S8.

Table S5. Quantifications of the global Si inventory in the surface ocean (left column) and the C export from the surface ocean.

PI	Surface Si (Pg)	C EP via biogenic Si (Pg year^{-1})	C EP via detritus (Pg year^{-1})
Control	37.1	3.2	0.3
VarP:N	36.1	3.9	0.2
VarSi:N	22.6	1.5	0.2
Tuned	22.4	1.6	0.2
LGM			
Control	24.0	2.4	0.2
VarP:N	23.5	3.0	0.2

VarSi:N	16.4	1.6	0.1
Tuned	16.4	1.7	0.1

Note. Total ocean Si inventories are ~9039 Pg but vary little between experiments. The middle column assumes organic matter adheres to the diatom siliceous frustules, while the right column assumes all soft organic matter sinks independently.

The EP of exclusively soft P_{Diat} POM, exported through the detritus inventory, at the bottom of the euphotic zone (120 m) and is ~5 - 10% of the P_{Diat} C export when assuming adhesion to fast-sinking frustules (Table S5). Without the frustules, P_{Diat} EP reduced by ~0.08 Pg C year^{-1} (~35%) from PI *VarSi:N*, instead of the ~2.4 Pg C year^{-1} reduction (~62%) with the accelerated sinking. The model may also be notably underestimating the P_{Diat} C EP in all simulations and may have notable implications for the C export quantifications and atmospheric CO_2 changes between climate states.

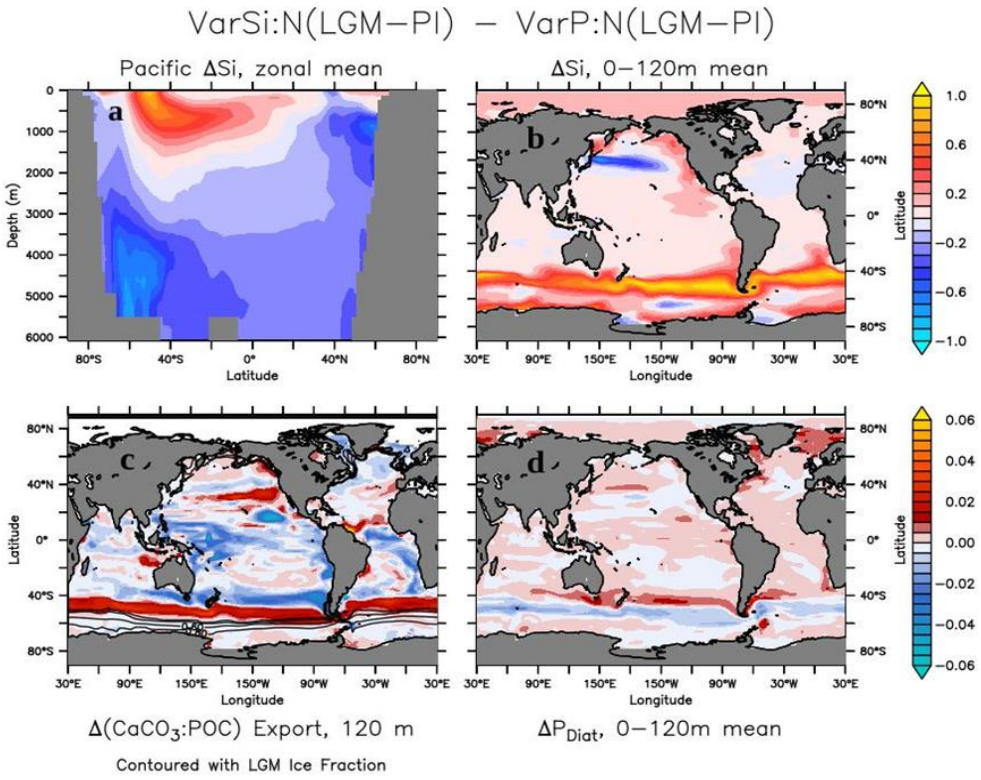

Figure S18. Silica leakage from the Southern Ocean in the LGM. The Pacific sector cross-section (a) and surface map (b) are in units of grams of Si m^{-3}and show the transport of Si from the SO to the equatorial East Pacific. The $CaCO_3$:POC export ratio

(c) and contoured sea ice fraction are unitless. Changes in P_{Diat} are in grams of C m^{-3}. All panels show the difference between VarSi:N's and VarP:N's LGM to PI change, thus removing the climate shift's effect on the selected variables and allowing exclusive visualization of the VarSi:N's influence on the Si cycle.

Text S4. Effects of Reduced Sedimentary Fe Fluxes in the LGM

With the formation of massive ice sheets in the LGM came lower sea levels (~ 125 m) (Lambeck et al., 2014; Muglia et al., 2018). The exposed continental shelves caused a reduction of the sedimentary Fe fluxes into the ocean (Muglia et al., 2017). The model configurations used in this study neglect an interactive ocean sediment module. Particulate organic matter (POM) is then instantaneously remineralized into the adjacent grid cell when it intersects the seafloor. We explored the effects of the altered ocean basin geometry in the LGM by including a recalculated sub-grid bathymetry (SGB) map for the LGM, but we emphasize there are large uncertainties in the model's Fe cycle, as well as the parameterization of the sedimentary Fe flux rates, which rely on constant stoichiometric ratios (Galbraith et al., 2010; Muglia et al., 2017, 2018; Tagliabue et al., 2009). Muglia et al. (2017) discuss in detail the potential limitations of the model's LGM Fe cycling.

The effects of the recalculated Fe sedimentary fluxes (Table S6) here are broadly consistent with those found by Muglia et al. (2017). The recalculated bathymetry map reduced the global ocean and euphotic zone Fe inventory but has notable implications when considering variable stoichiometry and the population dynamics of ocean primary producers. Of course, a reduction in euphotic zone Fe leads to reduced primary production, but when combined with *VarP:N* it also reduced the P_O-P_{Diaz} cohabitation (discussed in the main manuscript) thus reducing total NPP further. The revised sedimentary Fe fluxes expand the Fe limitation for all primary producers (see Figure S19). Ultimately, this leads to a reduction in C EP and reduced efficiency of the biological carbon pump which yields a smaller PI-to-LGM CO_2 drawdown and higher simulated LGM atmospheric CO_2 concentrations.

Of the selected variables in Table S6, most change similarly in the *Control* and *Tuned* models in response to the new SGB. However, the N-fixations, denitrification, and phytoplankton variables change substantially, highlighting the Fe-sensitivity of the P_O-P_{Diaz} cohabitation. These variables, as shown in the main text, are important for C export and ocean inventory quantifications. There are, however, some improvements to the simulated $\delta^{15}N$ and $\delta^{13}C$ as compared to observations, Table S7. The notable changes to N-fixation and denitrification, as opposed to the comparatively small changes in biological C export, explain the more profound impact that the new SGB has on $\delta^{15}N$ representations as compared to the $\delta^{13}C$ representations.

Table S6. Comparison of selected parameters in response to adjusted LGM sedimentary Fe fluxes caused by lower sea levels.

Parameter	Control		Tuned		ΔControl	ΔTuned
	PI SGB	LGM SGB	PI SGB	LGM SGB		
Atmospheric CO_2 (ppm)	204.7	205.9	190.5	197.2	1.2	6.7
EP (Pg C $year^{-1}$)	7.1	6.9	8.3	7.9	-0.2	-0.4
Total Fe inventory (Tg)	61.3	59.5	61.8	58.8	-1.8	-3.0
Surface (0-120 m) Total Fe inventory (Tg)	1.3	1.1	1.1	0.9	-0.2	-0.2
N-Fixation (Tg $year^{-1}$)	145.9	100.8	224.3	108.3	-45.1	-116.0
Water Column Denitrification (Tg $year^{-1}$)	92.6	53.1	155.4	40.7	-39.5	-114.7
Benthic Denitrification (Tg $year^{-1}$)	66.5	58.7	86.3	69.1	-7.8	-17.1
Total NO_3 Inventory (Pg)	2615.4	2723.9	2848.5	2926	108.5	77.5
Surface (0-120 m) NO_3 (Pg)	8.8	9.7	12.6	13.5	0.9	0.9
P_O biomass (N Tmol)	3.0	2.9	7.5	5.6	-0.1	-1.9

Diazotroph Biomass (N Tmol)	0.2	0.1	0.4	0.2	0.0	-0.2

Note. PI SGB indicates that the ocean geometry remained that of the PI ocean during the LGM simulation, while the other column refers to the recalculated LGM bathymetry due to lower sea levels.

Thus, the influence of variable stoichiometry in ocean biogeochemical models can strongly depend on the configuration and accuracy of tertiary, biologically-relevant model components. Using a different Fe flux scheme substantially altered the modeled climate impacts our variable stoichiometry schemes had. It is alternatively possible that the inclusion of other earth system components in the model would diminish the importance of the SGB remineralization schemes. The variable stoichiometry influences will likely vary considerably in other global climate and/or ocean biogeochemical models. Further research and testing are needed to determine the sensitivity of these stoichiometry schemes to various biogeochemical processes.

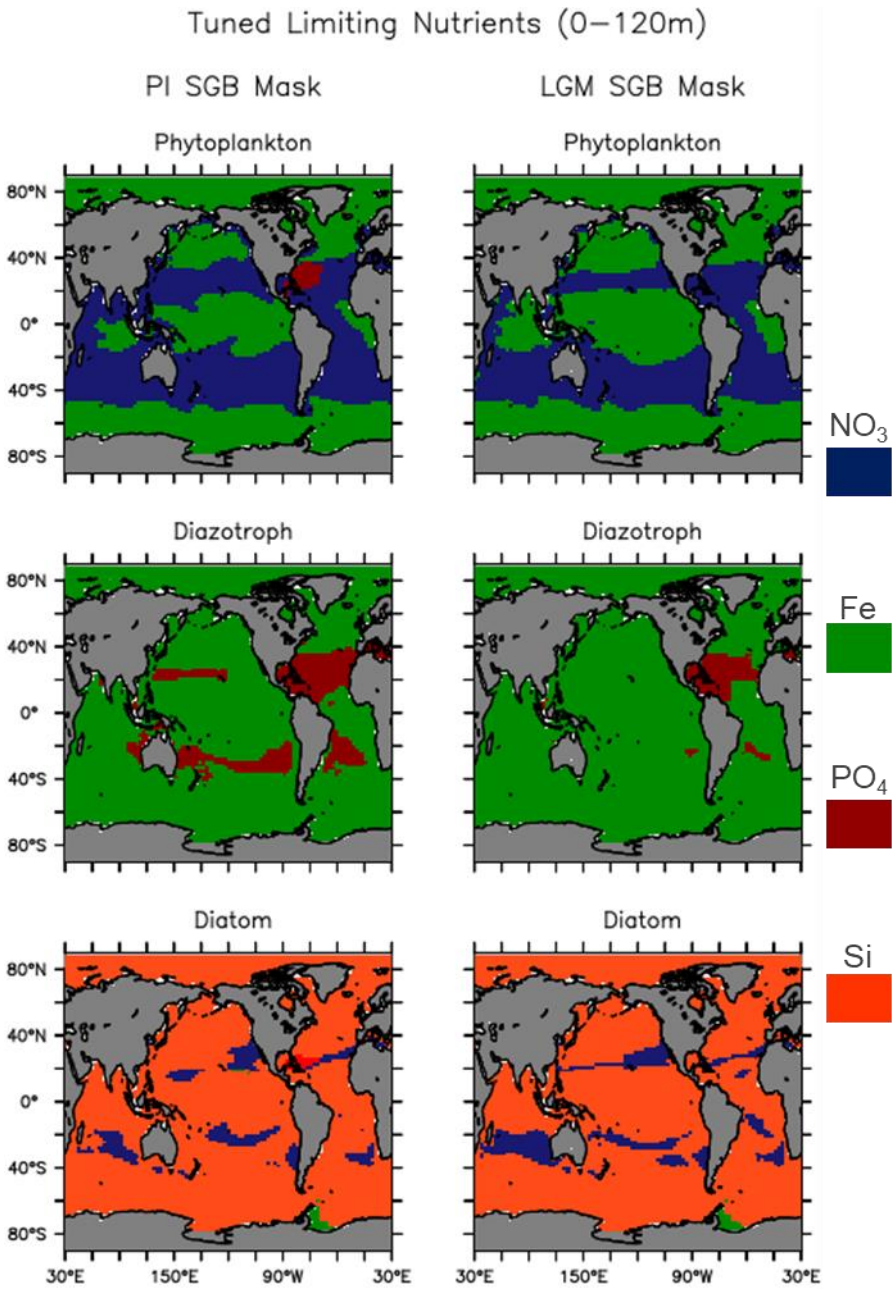

Figure S19. Comparison of each PFT limiting nutrients in response to changes in sedimentary Fe flux from lowered LGM sea levels and recalculated SGB. PI SGB configuration is on the left column and the LGM configuration is on the right. Both simulations are performed under identical LGM boundary conditions.

Text S5. Variable Stoichiometry Effects on $\delta^{15}N$

S5.1: Preindustrial

VarP:N caused a larger N NPP increase than P NPP. From the *Control*, *VarP:*N global N NPP increased by ~13% while P NPP increased by only 2%. *VarSi:N* did not change either NPP considerably, while the *Tuned* model added another 3 and 5% increase, respectively (See Table 3 in main text). An increase in primary production consequently causes increased respiration, altering the O_2 concentrations at depth, thereby changing denitrification rates (Figure S7, S22, and S24) (Somes et al., 2010). Each of these processes uniquely fractionate N isotopes, thus, $\delta^{15}N$ values, which are used to constrain the model, are heavily influenced by variable stoichiometry (Schmittner & Somes, 2016; Somes et al., 2010). The VSMs did not substantially improve simulations of N isotopic ratios. In low oxygen areas, the increased export drives notable inaccuracies in simulated $\delta^{15}N$ values. Many of these are corrected in the *Tuned* simulation.

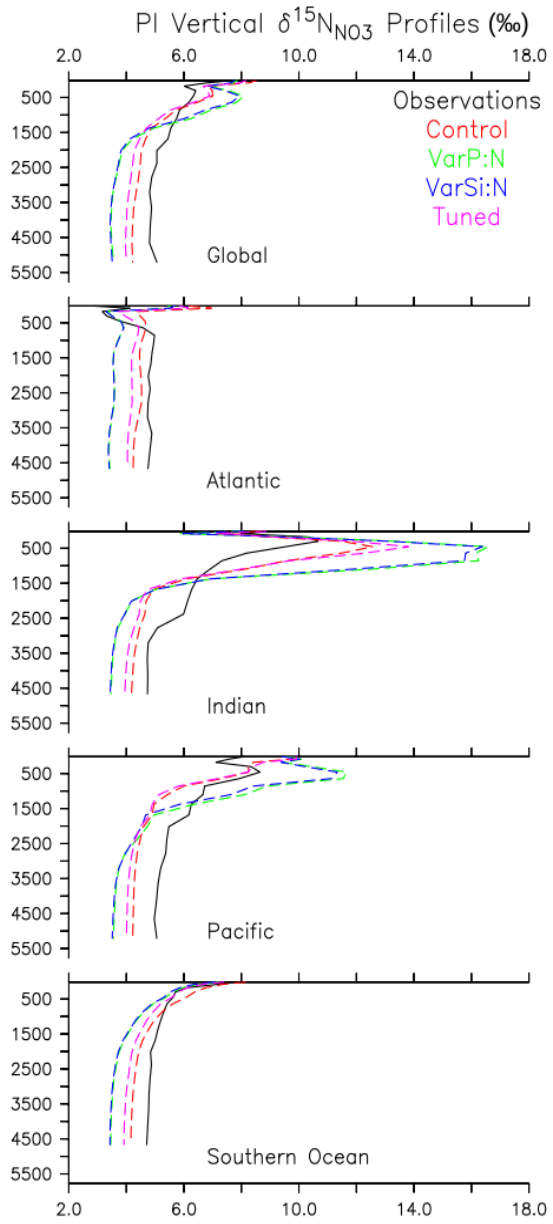

Figure S20. Vertical profiles of horizontally averaged $\delta^{15}N$ in the preindustrial ocean.

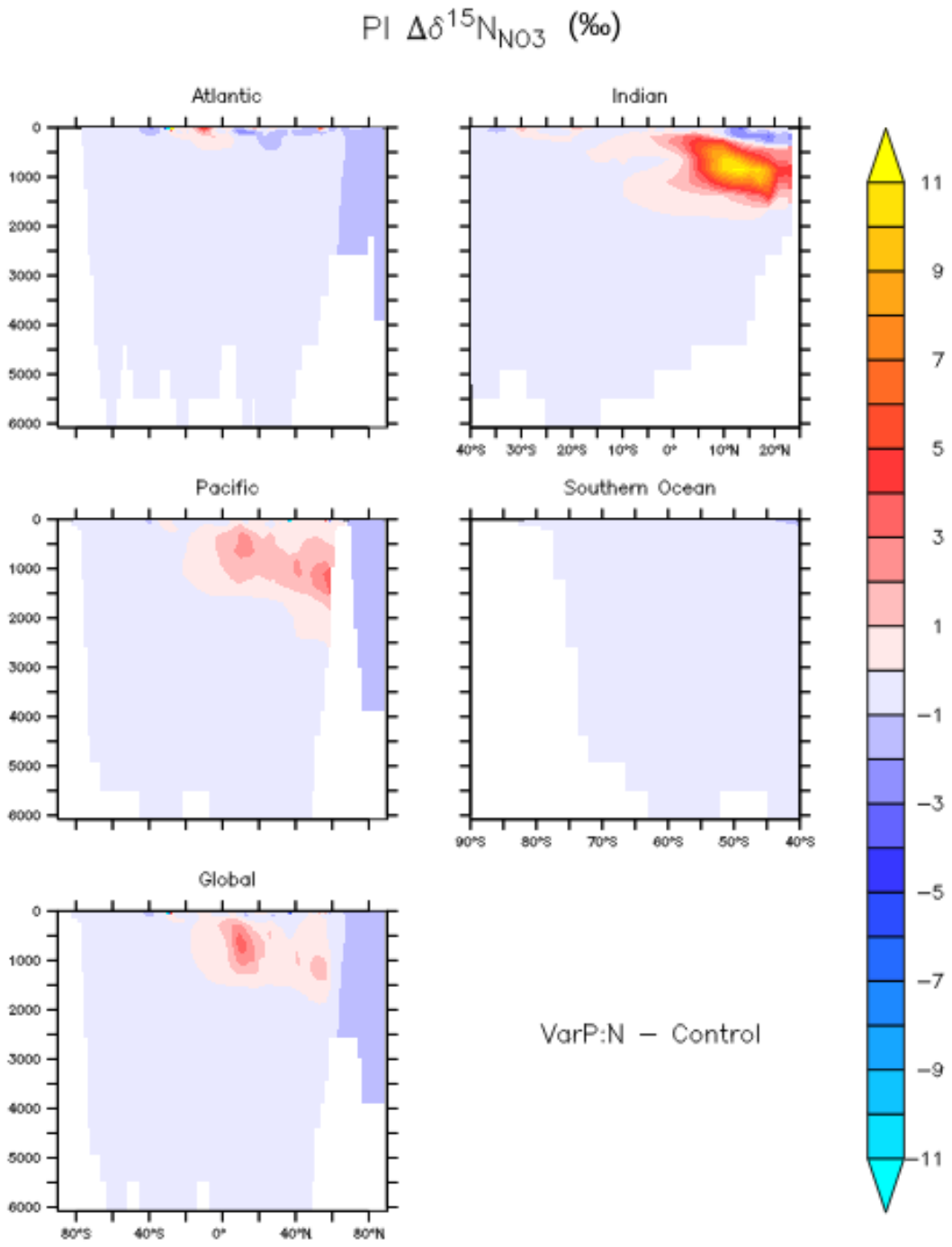

Figure S21. Changes in the $\delta^{15}N$ of NO_3 in response to VarP:N in the preindustrial ocean basins.

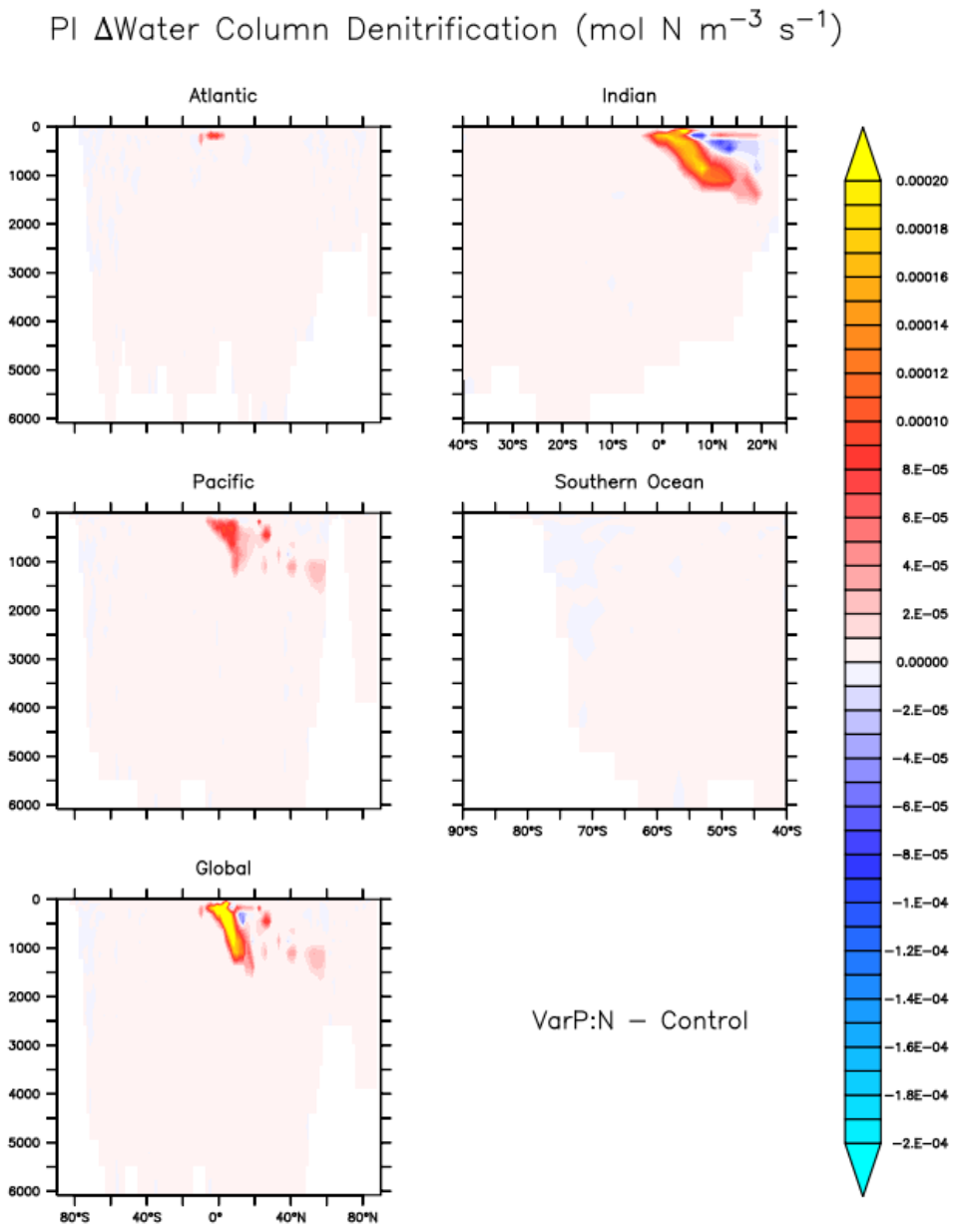

Figure S22. Changes in the water column denitrification in response to VarP:N in the PI ocean basins.

Against observed values, *VarP:N* and *VarSi:N* improve $\delta^{15}N$ simulations in the upper Atlantic and Southern Oceans, above ~500 m, however, both overestimate values in the upper Indian and Pacific (Figure S20) (Somes et al., 2010). These overestimations correlate with regions of low oxygen, suggesting that the increased export of organic matter in *VarP:N* and *VarSi:N* is too high in these areas which subsequently yields too

much denitrification that strongly increases $\delta^{15}N$ values (Figures S21 and S22). Similar effects on $\delta^{15}N$ was observed in the CSIRO model (Buchanan et al., 2019). The accelerated remineralization of the *Tuned* experiment corrects these overestimations in the upper Indian and Pacific Ocean basins, generally outperforming the *Control* simulation. All experiments underestimate $\delta^{15}N$ at depth; the deep ocean values are similar across each basin but remain sensitive to the soft tissue pump as the enhancement of the EP from the VSMs causes preferential export of ^{14}N. Here, the *Tuned* simulation does not best the *Control* but is only slightly less accurate (Table S7). $\delta^{15}N$ data for the PI and LGM were compiled and compared against the *Control* model performance in previous works (Muglia et al., 2018; Schmittner & Somes, 2016; Somes et al., 2010).

Table S7. Statistical performance of simulated $\delta^{15}N$ and $\delta^{13}C$. Note the PI comparison is representative of the whole ocean volume.

PI $\delta^{15}N$:	**R**	**STDR**	**RMS Prime**	**RMSE**
Control	0.75	1.26	0.84	0.84
VarP:N	0.77	2.16	1.53	1.53
VarSi:N	0.77	2.09	1.46	1.47
Tuned	0.75	1.30	0.86	0.88
LGM $\delta^{15}N$:				
Control	0.09	1.24	1.53	1.68
Control + SGB	0.15	1.02	1.31	1.61
VarP:N	0.05	1.94	2.14	2.26
VarSi:N	0.06	2.02	2.20	2.28
Tuned	0.06	1.67	1.90	1.98
Tuned + SGB	0.23	1.08	1.29	1.66
LGM $\delta^{13}C$:				
Control	0.79	0.97	0.64	0.65
Control + SGB	0.79	0.96	0.63	0.64
Tuned	0.79	0.97	0.64	0.74
Tuned + SGB	0.79	0.92	0.62	0.63

Note. Conversely, the LGM comparison is only representative of the surface ocean from where the bulk organic matter measured in the sediment cores originates. Values for each parameter are calculated as described in Muglia et al. (2018).

S5.2: LGM

LGM $\delta^{15}N$ data, while spatially limited, represents the cumulative interplay between surface ocean $\delta^{15}N$ values and subsequent fractionation by biological processes (Galbraith et al., 2013; Tesdal et al., 2013). Sedimented organic matter isotopic

signatures are exemplary of surface signatures and so the $\delta^{15}N$ of simulated detritus is compared to LGM data (Tesdal et al., 2013). The *Control* experiment mainly errs with overestimations of $\delta^{15}N$ values in the surface North Pacific and Bering Sea by ~2-4‰ compared to the 5‰ of observations (Figure S23). *VarP:N* increases $\delta^{15}N$ by an additional 2‰, causing a significant overestimation for most of the North Pacific. *VarP:N* also causes strong $\delta^{15}N$ increases, ~9‰, off southern Central America and the Arabian Sea from the observed 9‰ and 5‰ values, respectively (Figure S23). Similar to the PI simulations, *VarSi:N* shows little effect on the $\delta^{15}N$ values, whereas the *Tuned* simulation corrects the large overestimation caused by *VarP:N* in the North Pacific and Bering Sea. The $\delta^{15}N$ values are reduced below those of the LGM *Control* and are in better agreement with the observed data, differing by ~1‰. $\delta^{15}N$ off southern Central America and the Arabian Sea values remain elevated.

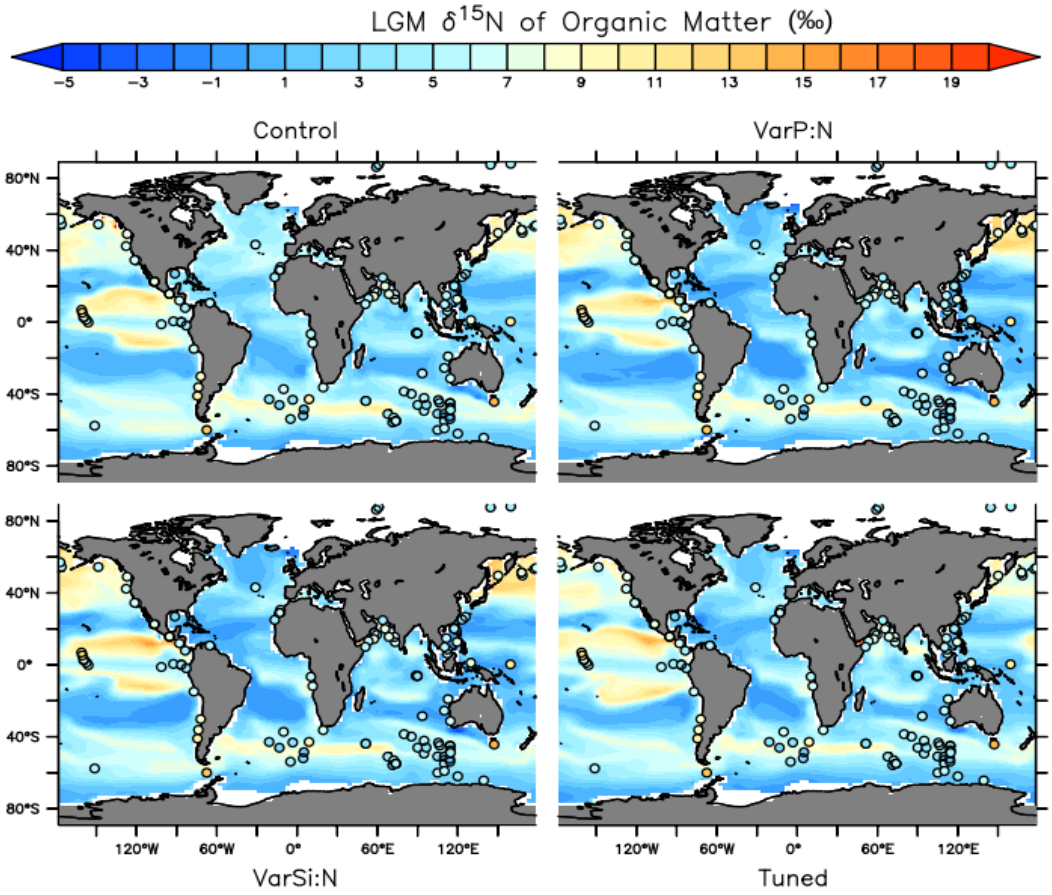

Figure S23. $\delta^{15}N$ of organic matter in the LGM averaged over the uppermost 120 m of the water column. Overlaid are observed values (Tesdal et al., 2013).

In the LGM North Pacific, the effects of *VarP:N* are exacerbated; water column denitrification nearly triples from the *Control* between the levels of 1250 – 4000m (Figure S25). $\delta^{15}N$ values here increased from 18 to ~42‰ (Figure S24). The *Tuned* model mitigates this strong $\delta^{15}N$ increase and is similar to the *Control* experiment's $\delta^{15}N$ in this region. A similar increase in denitrification is seen at this location in the PI but is notably weaker and less spatially extensive (Figures S21 and S24). The differences in $\delta^{15}N$ response to *VarP:N* between the PI and LGM oceans derive from the differences in NPP increases. In the PI ocean, *VarP:N* drove a 13% increase in N NPP compared to the *Control* run, while in the LGM, a 22% increase (Table 3 in the main text). Thus, the biological fractionation and denitrification influences on $\delta^{15}N$ vary.

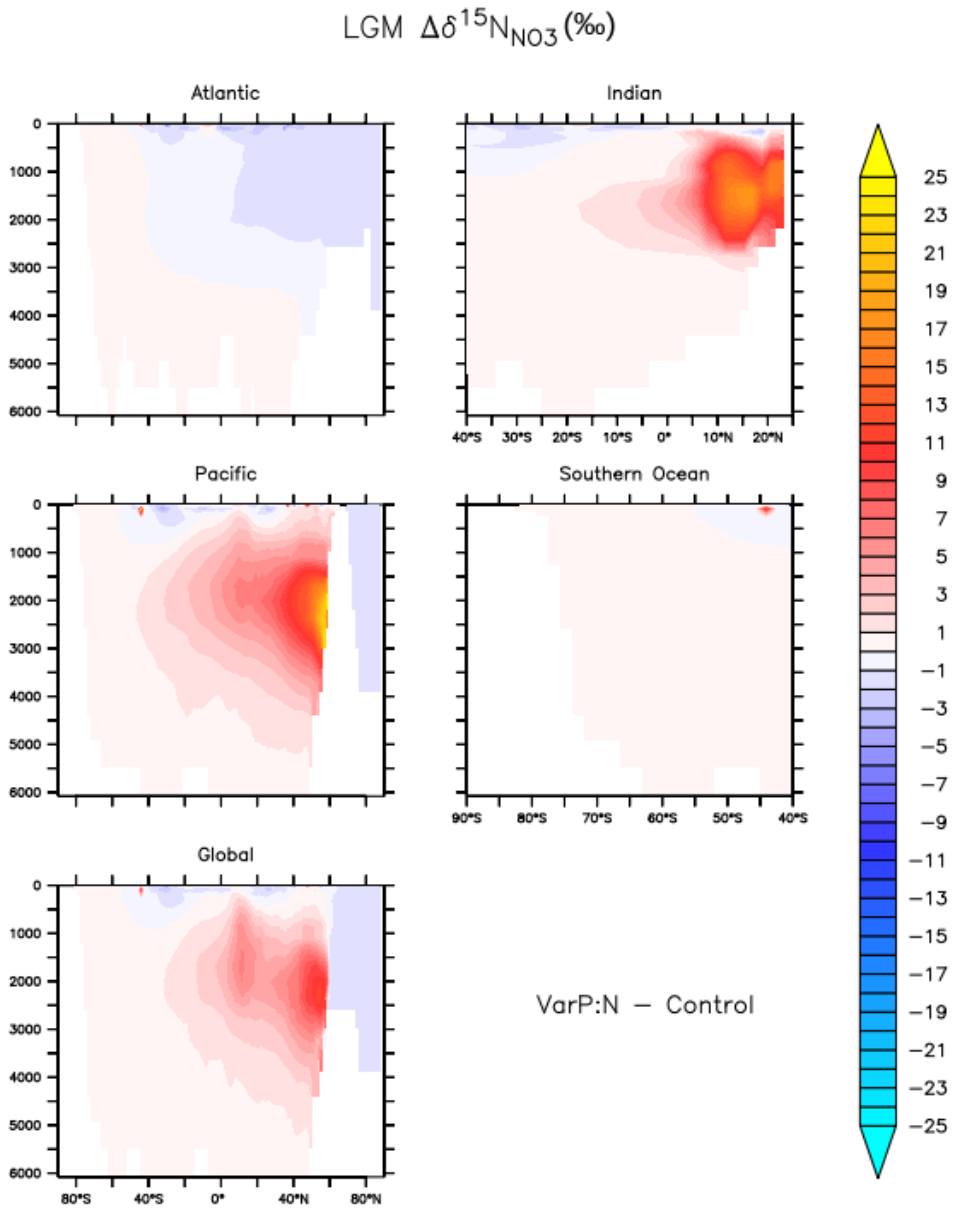

Figure S24. Changes in the $\delta^{15}N$ of NO_3 in response to VarP:N in the LGM ocean basins.

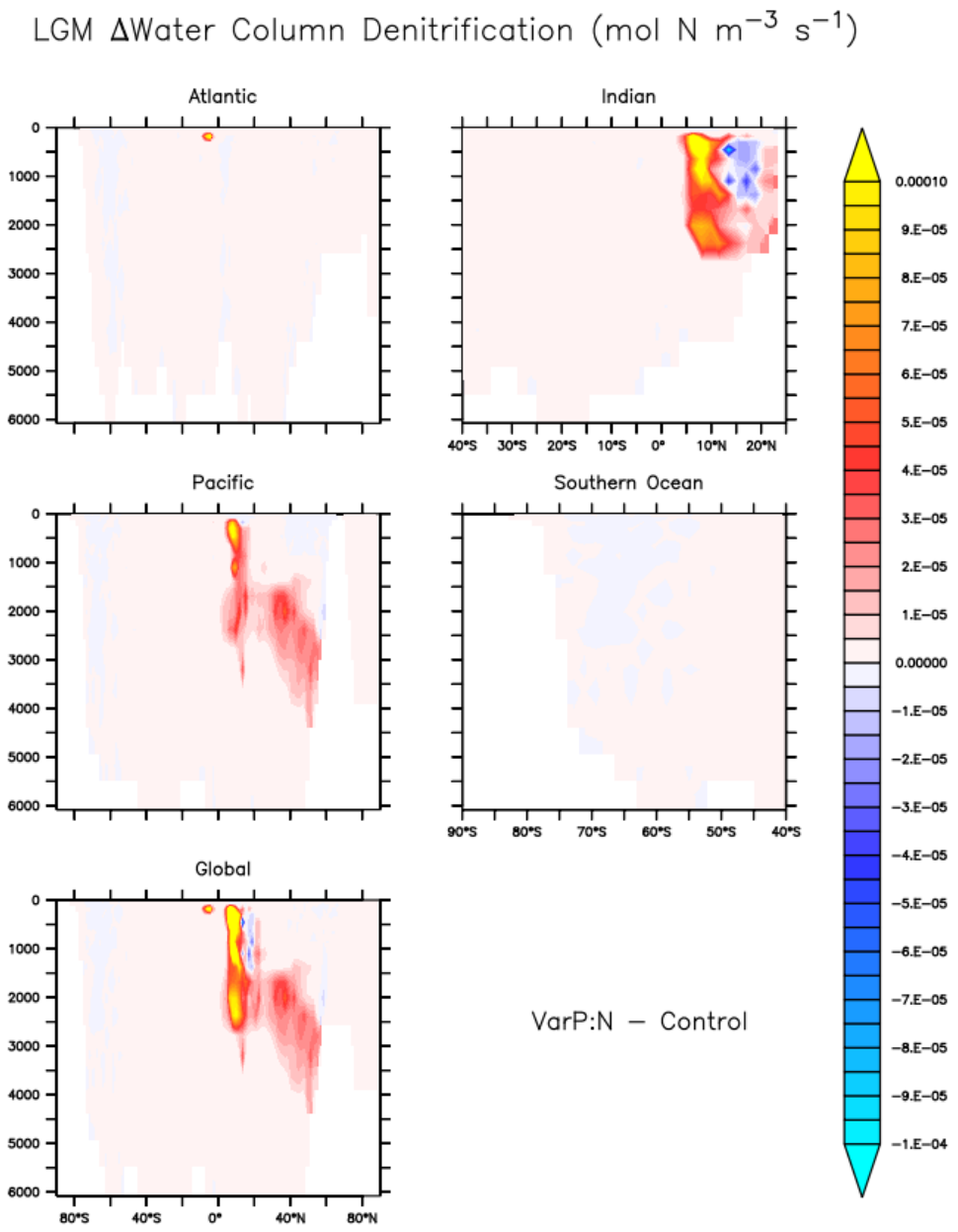

Figure S25. Changes in the water column denitrification in response to VarP:N in the LGM ocean basins.

Text S6. Biogeochemical Equations and Description

This section provides an explicit description of the new and revised prognostic equations for the implementation of the variable N:P scheme adapted from Galbraith and Martiny (2015). These are alterations of the MOBI equations in Somes and Oschlies (2015) with some portions described by external sources as referenced therein. The

inclusion of the variable N:P model necessitated two new prognostic equations to explicitly calculate the P content (indicated by the subscript "$\langle P \rangle$" of P_O and detritus (D) and a reconfiguration of the predictive PO_4 and DOP equations. The original N currency equation are noted with "$\langle N \rangle$". See Table S8 for variable and symbol descriptions.

S7.

$$\frac{\partial PO_4^{3-}}{\partial t} = \lambda_{DOP} DOP + \mu_D^* DR_{P:N_D} + R_{P:N}\left[\gamma P_z(1-\omega)\left(\frac{R_{N:P}}{R_{P:N_{DZ}}} G_{P_{DZ}}^* + \zeta_{P_O} G_{P_O}^* + G_{P_{DT}}^* + G_{P_Z}^* + \zeta_D G_D^*\right) + (1-\sigma 2_{DOM})\mu_{P_{DT}}^* P_{DT} - \left(1 - u_{DOP_{P_{DT}}}\right) J_{DT}^* P_{DT}\right] + R_{P:N_{P_O}}\left[(1-\sigma 2_{DOM})\mu_{P_O}^* P_O + u_{DOP_{P_O}} J_{P_o}^* P_O\right] - R_{GM15} J_{P_o}^* P_O - R_{P:N_{DZ}}\left(1 - u_{DOP_{P_{DZ}}}\right) J_{DZ}^* P_{DZ}$$

S8. Similar to Equation S7, nutrients are added to the DOP inventory at a ratio equal to the calculated N:P of P_O and detritus (S13). However, the uptake of DOP and DON is consumed at this same ratio, not by the GM15 N:P.

$$\frac{\partial DOP}{\partial t} = R_{P:N}\left[\sigma 1_{DOM} \upsilon_{P_{DT}} P_{DT} + \sigma 2_{DOM} \mu_{P_{DT}}^* P_{DT} - u_{DOP_{P_{DT}}} J_{DT}^* P_{DT}\right] + R_{P:N_{P_O}}\left(\sigma 1_{DOM} \upsilon_{P_O} P_O + \sigma 2_{DOM} \mu_{P_O}^* P_O - u_{DOP_{P_O}} J_{P_o}^* P_O\right) - R_{P:N_{DZ}} u_{DOP_{P_{DZ}}} J_{DZ}^* P_{DZ} - \lambda_{DOP} DOP$$

S9.

$$\frac{\partial P_{O_{\langle N \rangle}}}{\partial t} = J_{P_o}^* P_O - \mu_{P_O}^* P_O - \upsilon_{P_O} P_O - \zeta_{P_O} G_{P_O}^* P_z$$

S10. The P_O equation in the P currency is, again, sourced at a ratio to the N currency version that is determined by the GM15 N:P equation. Reductions to this inventory are at the N:P of the P_O.

$$\frac{\partial P_{O_{\langle P \rangle}}}{\partial t} = R_{GM15} J^*_{P_O} P_O - R_{P:N_{P_O}} \left(\mu^*_{P_O} P_O + \upsilon_{P_O} P_O + \zeta_{P_O} G^*_{P_O} P_z \right)$$

S11.

$$\frac{\partial D_{\langle N \rangle}}{\partial t} = (1-\gamma) P_z \left(G^*_{P_{DZ}} + \zeta G^*_{P_O} + G^*_{P_{DT}} + G^*_{P_Z} + \zeta G^*_D \right) + (1 - \sigma 1_{DOM}) \upsilon_{P_O} P_O - \mu^*_D D$$
$$- \zeta_D G^*_D P_z + (1 - \sigma 1_{DOM}) \upsilon_{P_{DT}} P_{DT} + \frac{R_{N:P}}{R_{N:P_{DZ}}} \upsilon_{P_{DZ}} P_{DZ} + \upsilon_{P_Z} P_Z^2 + w_D \frac{\partial D}{\partial z}$$

S12. The N:P of the prognostic detritus is determined by the weighted combination of the different plankton groups and post-grazing detrital matter.

$$\frac{\partial D_{\langle P \rangle}}{\partial t} = (1-\gamma) P_z \Big[R_{P:N} \left(G^*_{P_{DT}} + G^*_{P_Z} \right) + R_{P:N_{DZ}} G^*_{P_{DZ}} + \zeta_{P_O} G^*_{P_O} (R_{P:N_{P_O}} - \gamma R_{P:N})$$
$$+ \zeta_D G^*_D (R_{P:N_D} - \gamma R_{P:N}) \Big]$$
$$+ R_{P:N} \left[\upsilon_{P_Z} P_Z^2 + \frac{R_{N:P}}{R_{N:P_{DZ}}} \upsilon_{P_{DZ}} P_{DZ} + (1 - \sigma 1_{DOM}) \upsilon_{P_{DT}} P_{DT} \right]$$
$$+ R_{P:N_D} \left(w_D \frac{\partial D}{\partial z} - \zeta_D G^*_D P_z - \mu^*_D D \right) + R_{P:N_{P_O}} (1 - \sigma 1_{DOM}) \upsilon_{P_O} P_O$$

S13. Expression of the P_O and detritus P:N for each timestep and grid box.

$$R_{P:N_X} = \frac{X_{\langle P \rangle}}{X_{\langle N \rangle}},$$

where $X = [P_O, D]$.

S14. ζ acts to regulate the zooplankton grazing on P_O and detritus that are now under variable stoichiometry schemes. If a grazed particle is lacking in P, it is viewed as not nutritious, and the grazing is turned off. This was done to preserve the computational efficiency and realism of having fixed zooplankton stoichiometry without having unrealistic instantaneous remineralization of organic matter into inorganic nutrient constituents.

$$\zeta_X = \begin{cases} R_{P:N_X} \geq \gamma R_{P:N} \; ; \;\; \zeta_X = 1 \\ R_{P:N_X} < \gamma R_{P:N} \; ; \;\; \zeta_X = 0 \end{cases}.$$

Table S8. List of biogeochemical variables, their symbols, values, and units.

Variable/Description	Symbol	Value	Units
Ordinary Phytoplankton	P_O	-	mol m^{-3}
Diazotrophs	P_{Diaz}	-	mol m^{-3}
Diatoms	P_{Diat}	-	mol m^{-3}
Zooplankton	P_Z	-	mol m^{-3}
Detritus	D	-	mol m^{-3}
DOP remineralization rate	λ_{DOP}	-	day^{-1}
DON remineralization rate	λ_{DON}	-	day^{-1}
Detritus remineralization rate	μ_D^*	-	day^{-1}
Zooplankton assimilation efficiency	γ	0.7	day^{-1}
Zooplankton growth efficiency	ω	0.54	-
Grazing rate	G^*	-	-
Selective grazing regulator	ζ	0, 1	-
Fraction of phytoplankton mortality routed to DOM	$\sigma 1$	0.1	-
Fraction of microbial fast-recycling routed to DOM	$\sigma 2$	0.08	-
Quadratic mortality rate	υ	-	day^{-1}
Specific mortality rate	μ^*		day^{-1}
Phosphorus uptake source regulator	u_{DOP}	0, J^*	-
Growth rate	J^*	-	-
Variable P:N uptake as defined by GM15	R_{GM15}	-	mol mol^{-1}
Redfield P:N	$R_{P:N}$	1/16	mol mol^{-1}
Diazotroph P:N	$R_{P:N_{DZ}}$	1/40	mol mol^{-1}
Variable traced in N units	<N>	-	-
Variable traced in P units	<P>	-	-
Sinking Velocity of POM	w_D	-	s^{-1}

Note. A "-" in the value column indicates that the item is variable as a function of nutrient availability, temperature, etc. (Somes & Oschlies, 2015).